

Revision

1 **Aluminum ordering and clustering in Al-rich synthetic phlogopite: The**
2 **influence of fluorine investigated by $\{^{19}\text{F}/^1\text{H}\}$ ^{29}Si CPMAS NMR**
3 **spectroscopy**

4
5
6 **MICHAEL FECHTELKORD^{*}, RAMONA LANGNER[†]**

7
8
9 Institut für Geologie, Mineralogie und Geophysik, Ruhr-Universität Bochum,
10 Universitätsstr. 150, 44780 Bochum, Germany

11
12
13
14
15

*E-mail: Michael.Fechtelkord@ruhr-uni-bochum.de

[†]Present address: Fraunhofer-Institut für Naturwissenschaftlich-Technische Trendanaly-
sen (INT), Appellsgarten 2, 53879 Euskirchen, Germany

Revision #3

16

ABSTRACT

17

18 The influence of fluorine on cationic and anionic ordering in the mica mineral
19 phlogopite has been investigated using ^{29}Si , ^1H , and ^{19}F MAS as well as $\{^1\text{H}\}/\{^{19}\text{F}\} \rightarrow$
20 ^{29}Si CPMAS and CP-depolarization NMR spectroscopies. It can be shown that the mere
21 presence of fluorine achieves a tremendous loss of capability to incorporate aluminum
22 into the phlogopite structure. Fluorine is usually located in Mg-rich octahedral and Si-
23 rich tetrahedral clusters of the phlogopite structure while hydroxyl groups are located in
24 Al-rich octahedral and tetrahedral clusters as derived from $\{^1\text{H}\}/\{^{19}\text{F}\} \rightarrow ^{29}\text{Si}$ CPMAS
25 NMR spectroscopies. The ordering effect in these two basic structural clusters can also
26 be proven by a smaller ^{29}Si linewidth in the $\{^{19}\text{F}\} \rightarrow ^{29}\text{Si}$ CPMAS NMR experiments
27 compared to the usual ^{29}Si MAS NMR experiment showing a stronger ordering of Si –
28 environments near the two different anion types fluorine and hydroxyl. Intensities of the
29 $\{^1\text{H}\}/\{^{19}\text{F}\} \rightarrow ^{29}\text{Si}$ CPMAS NMR signals as function of the contact-time show a
30 deviation from the classical I-S model and can be attributed to the I-I* -S model. Time
31 constants like the proton/fluorine spin diffusion time (T_{df}), the spin-spin relaxation time
32 (T_2), the lambda parameter (λ), and the proton/fluorine spin-lattice time in the rotating
33 frame ($T_{1\rho}$) were extracted to give information about the local structure.

34

35 **KEYWORDS:** ^1H / ^{19}F / ^{29}Si / Solid State NMR / MAS / CPMAS /
36 DEPOLARIZATION / phlogopite / fluorine

Revision #3

37

38

INTRODUCTION

39 F is often present in silicic magmas only in minor amounts, but it may be strongly
40 enriched in the melt during on-going crystallization because of its incompatible
41 character. As a result, F-rich minerals like phlogopite form in late-stage magmatic rocks
42 like pegmatites (e.g., Christiansen et al. 1983; London 1987). For certain A-type
43 granites, F-contents up to 1.8 wt% have been found (Whalen et al. 1987), and even
44 larger amounts of 3.2 wt% F have been reported for topaz rhyolites by Pichavant and
45 Manning (1984). These amounts may have a strong influence on the physical and
46 chemical properties of magma with effects similar to those of water dissolved in the
47 melt. F lowers the crystallization temperature of a melt (Manning 1981; Webster et al.
48 1987; Weidner and Martin, 1987), it decreases the melt density (Dingwell et al. 1993;
49 Knoche et al. 1995) and melt viscosity (Dingwell et al. 1985; Baker and Vaillancourt
50 1995; Giordano et al. 2004), and increases element diffusivity in the melt (Baker and
51 Bossányi 1994). However, there is an important difference in the behavior of F and
52 H₂O: The water solubility decreases upon ascent of the magma, leading to a higher
53 viscosity and higher solidus temperatures, and thus a more explosive nature of
54 eruptions. In contrast, the fluorine solubility may still achieve several wt% of fluorine
55 even at low pressures, inhibiting degassing upon extrusion, corresponding to a
56 completely different behavior of the melt (Carroll and Webster 1994).

57 Therefore, it is essential to gain a deeper understanding of the stability of such F-rich
58 minerals and the processes controlling a partitioning of F between mineral and co-
59 existing melt. This includes studies of phase equilibria, partitioning coefficients and
60 thermal stability of micas. It is also necessary to obtain further information on the local

Revision #3

61 F-environment in the melt as well as in the F-containing crystal structures. In contrast to
62 standard techniques like X-ray and neutron diffraction, spectroscopic methods are ideal
63 tools to obtain information on the local environment of single atoms in the structure.

64 The mica mineral phlogopite shows an extraordinary capability to incorporate larger
65 amounts of F than most other minerals. Within the class of mica minerals this is only
66 exceeded by the Li-mica lepidolite (Foster 1960). Phlogopite is the Mg-end-member of
67 the biotite solid-solution series with composition $K Mg_3 (AlSi_3O_{10}) (OH, F)_2$. The
68 mineral structure is made up of two-dimensional infinite octahedral sheets sandwiched
69 by two sheets of TO_4 -tetrahedra. Three of the four tetrahedral sites per half unit-cell in
70 phlogopite are occupied by Si and the remaining site by Al. Potassium ions occupy the
71 interlayer sections for charge balancing. In nature, extensive replacement of Si and Mg
72 by Al according to Tschermak's substitution ($[^6]Mg + [^4]Si \rightarrow [^6]Al + [^4]Al$) takes place.
73 The composition then ranges towards the hypothetical end-member eastonite (K
74 $(Mg_2Al) (Al_2Si_2O_{10}) (OH, F)_2$).

75 In pure phlogopite the octahedral sites are occupied by Mg (three sites per half unit
76 cell). Two Mg sites are coordinated by four O atoms from the tetrahedral sheets and two
77 $(OH)^-$ and/or F^- anions in cis-coordination. The third Mg site has a trans-coordination of
78 the hydroxyl and/or F^- anions. The $(OH)^-$ and/or F^- anions are always coordinated to
79 three Mg-sites. In the Al-rich phlogopites, some of the Mg sites are substituted by Al, so
80 that some of the $(OH)^-$ and/or F^- anions are coordinated by two Mg cations and one Al
81 cation.

82 In their IR spectroscopic study, Papin et al. (1997) demonstrated that the OH/F
83 distribution in Al-rich phlogopite is not statistically random, but that the hydroxyl
84 groups prefer Mg_2Al coordination and the fluorine atoms prefer Mg_3 coordination. This

Revision #3

85 is in agreement with a previous ^{19}F , ^1H , and ^{29}Si MAS NMR study (Fechtelkord et al.
86 2003a). The results of this study indicated a non-statistical distribution of cations and
87 anions in the octahedral sheets where F prefers sites coordinated by three Mg, whereas
88 OH prefers sites bonded to Al. In addition, it was shown that hydroxyl-rich
89 compositions indicate an increased Al-content in the tetrahedral sheets suggesting a
90 stabilizing effect on the formation of Al-rich phlogopite and for fluorine rich
91 compositions a stabilizing effect on the formation of Mg-rich phlogopite (Fechtelkord et
92 al. 2003a; Circone et al. 1991).

93 In another study, $\{^1\text{H}\} \rightarrow ^{27}\text{Al}$ 2D CPMAS (HETCOR) NMR experiments at short
94 contact times showed information about the local configuration of tetrahedral Al sites
95 and Mg_3OH as well as Mg_2AlOH sites whereas magnetization was only transferred to
96 the octahedral Al sites from hydroxyl groups in Mg_2AlOH sites (Fechtelkord et al.
97 2003b). The $\{^{19}\text{F}\} \rightarrow ^{27}\text{Al}$ 2D CPMAS (HETCOR) NMR spectrum in Fechtelkord et al.
98 (2003b) was dominated by $^{\text{IV}}\text{Al}$ sites coupled to the Mg_3F complex in phlogopite.
99 Resonances from Mg_2AlF complexes were not observed. Finally, the $\{^1\text{H}/^{19}\text{F}\} ^{27}\text{Al}$
100 REDOR experiments in this study supported the results of the 2D CPMAS (HETCOR)
101 experiments. The slope of each REDOR curve gave a good hint about the strength of
102 heteronuclear dipolar coupling between Al and F or Al and H. The dipolar coupling
103 between the octahedral sites and OH/F should be stronger due to the smaller distance to
104 OH and fluorine groups compared to $^{\text{IV}}\text{Al}$ sites. The trend could be observed for all the
105 REDOR curves. The slope of the octahedral REDOR curves was always higher than for
106 the tetrahedral curve. In addition, $\{^1\text{H}\} \leftrightarrow ^{27}\text{Al}$ dipolar interaction is stronger than the
107 $\{^{19}\text{F}\} \leftrightarrow ^{27}\text{Al}$ dipolar interaction due to the higher gyromagnetic ratio of ^1H which could
108 be also observed in the graphs resulting in an increased slope for the $\{^1\text{H}\} ^{27}\text{Al}$ REDOR

Revision #3

109 curves compared to the $\{^{19}\text{F}\} \text{ }^{27}\text{Al}$ REDOR curves (Fechtelkord et al. 2003b). It was not
110 possible to extract quantitative information from the REDOR curves due to the lack of
111 enough data points in the initial slope.

112 In a recent work (Langner et al. 2012) we showed that different ordering schemes can
113 be found in the tetrahedral and octahedral sheets of phlogopite: In the tetrahedral sheet
114 ordering patterns are dominated by short-range ordering in order to avoid the formation
115 of Al-O-Al linkages following Loewenstein's rule (Loewenstein 1954). Long-range
116 ordering is only present at Al-content close to $\text{Si}/^{[4]}\text{Al} = 1:1$ with Al and Si occupying
117 the tetrahedra alternately. For the octahedral sheet an Al-O-Al avoidance similar to that
118 of the tetrahedral sheets has been found, and Al is always surrounded by six Mg ions in
119 the neighboring octahedra. There is a relationship between the ordering in both types of
120 sheets in that Al-atoms in the octahedral and the tetrahedral sheets tend to be located
121 next to each other forming Al-rich clusters in the structure.

122 However, these observations have been made on pure OH-phlogopites, so the
123 question now arises whether the clustering of Al in the structure also influences the
124 distribution of F and OH in F-rich phlogopites as one would expect from the OH-Al
125 preference mentioned above.

126 $\{^1\text{H}\}/\{^{19}\text{F}\} \rightarrow ^{29}\text{Si}$ cross-polarization magic-angle spinning (CPMAS) experiments
127 combined with ^1H , ^{19}F , and ^{29}Si MAS NMR investigations are an ideal tool to correlate
128 octahedral H or F environments with Si-environments in the tetrahedral sheets. The
129 correlation of octahedral and tetrahedral Al with octahedral H or F environments was
130 already done in a former study described above (Fechtelkord et al. 2003b). It can be
131 shown that the ordering of cations and anions is coupled with F preferring sites in the
132 Si-rich clusters in the structure. Moreover, the analysis of $\{^1\text{H}\}/\{^{19}\text{F}\} \rightarrow ^{29}\text{Si}$ contact-

Revision #3

133 time dependent CP and depolarization experiments (Pines et al. 1971, 1973;
134 Kolodziejcki and Klinowski 2002; Wu et al. 1988) provide relaxation, spin-diffusion,
135 and cross-polarization parameters, which contain valuable information on dynamics and
136 the local neighborhood between protons/fluorine anions and silicon atoms.

137 A number of phlogopite samples with nominal composition
138 $K(Mg_{3-x}Al_x)(Al_{1+x}Si_{3-x}O_{10})(OH)_yF_{2-y}$ have been prepared under synthesis conditions
139 of 873 K and 2 kbar to investigate the role of F on the ordering patterns in both sheets of
140 the phlogopite structure. In contrast to previous studies (e.g., Langner et al. 2012;
141 Circone et al. 1991), samples containing different amounts of fluorine ($y = 0.2 - 1.8$)
142 have been compared to samples of pure hydroxyl-phlogopite ($y = 2.0$).

143 In addition to the variation in the F-content, samples of different Al-contents $x = 0.0 -$
144 1.6 have been synthesized. Theoretically, the limit for incorporation of Al into the
145 phlogopite structure is $x = 1.0$ because then a ratio of $Si^{[4]}Al$ of 1:1 is reached.
146 Incorporating further Al into the tetrahedral sheets would force Al-atoms to occupy
147 neighboring tetrahedra which is expected to be highly energetically unfavorable
148 (Loewenstein 1954). However, values of x_{nom} higher than 1.0 have been chosen for the
149 preparation of gels because not all of the Al present in the initial gel composition is
150 incorporated into the phlogopite structure.

151

152 **EXPERIMENTAL METHODS**

153 Phlogopites of nominal composition $K(Mg_{3-x}Al_x)(Al_{1+x}Si_{3-x}O_{10})(OH)_yF_{2-y}$ with $x_{nom} =$
154 $0.0 - 1.6$ and $y = 0.2 - 2.0$ were synthesized using sol-gel-synthesis and hydrothermal
155 techniques. Starting materials for the Al-rich F-containing phlogopites were prepared

Revision #3

156 according to the gelling method of Hamilton and Henderson (1968). The F anions were
157 introduced by adding 1 M NH₄F solution to the starting gel solution in the appropriate
158 amounts. A typical experiment consisted of 150-300 mg of the dry gel together with 9-
159 12 wt% of deionized water in a sealed gold capsule (40 mm long and 3.5 mm inner
160 diameter). Experiments were carried out in Tuttle-type cold seal pressure vessels at
161 1073 K or 873 K and 2 kbar for a duration of 7 days using water as pressure medium
162 (for detailed description of the vessels see Berndt et al. 2001). The value of $f(O_2)$ was
163 close to that imposed by the Ni-NiO buffer.

164 The chemical composition of the dry oxide gels was checked for several samples by
165 wavelength dispersive X-ray fluorescence spectroscopy (XRF) on a Philips PW 2404
166 spectrometer equipped with an Rh X-ray tube. Oxides were mixed with LiBO₂/Li₂B₄O₇
167 (MERCK Spectromelt A12) in a ratio of 1:10 in a fused bead. Analysis results showed
168 no major deviations from the intended stoichiometry of the gels.

169 After synthesis the samples have been checked with powder X-ray diffraction on a
170 D8 Bruker diffractometer. Two phlogopite polytypes have been identified: At low Al-
171 contents polytypes 1M and 2M₁ co-exist, while at high Al-contents nearly pure
172 phlogopite-2M₁ has been found. In agreement with ²⁷Al MAS NMR experiments
173 corundum has been observed as an impurity phase as well as potassium aluminum
174 hexafluoride (K₃AlF₆·0.5H₂O) (mainly at high fluorine and aluminum contents). On the
175 other hand, the chemical composition of the phlogopite was difficult to estimate, e.g.,
176 by microprobe analysis. The average crystal size is about 1 - 2 μm and the crystals were
177 generally oriented with their thinnest side parallel to the plane of the thin section. In
178 addition, the thin section often contained large cavities between the phlogopite crystals
179 filled by epoxy resin so that analytical totals were too low to be used.

Revision #3

180 The NMR spectra were recorded on a Bruker ASX 400 NMR spectrometer.
181 ^{29}Si MAS NMR measurements were carried out at 79.49 MHz using a standard Bruker
182 7 mm MAS NMR probe with sample spinning at 4.0 kHz, a single pulse duration of
183 $2\ \mu\text{s}$ (90° pulse length $5.8\ \mu\text{s}$) and 4,000 - 20,000 scans were accumulated with a 10 s
184 recycle delay. To ensure that the 10 s delay is sufficient with regard to spin-lattice
185 relaxation times (T_1), some experiments were repeated with a delay of 120 s, but no
186 change in absolute intensity could be observed. Tetramethylsilane was used as reference
187 standard. In addition, high-power-decoupled $\{^1\text{H}/^{19}\text{F}\} - ^{29}\text{Si}$ MAS NMR experiments
188 were carried out to check the dependence of ^{29}Si signal linewidths on $^1\text{H}/^{19}\text{F} - ^{29}\text{Si}$
189 heteronuclear dipolar interaction.

190 ^1H MAS NMR experiments have been performed at 400.13 MHz with a standard
191 Bruker 4 mm MAS NMR probe at rotation frequencies of 12.5 kHz. Liquid
192 tetramethylsilane (TMS) was used as an external standard. A pulse length of $2\ \mu\text{s}$ and a
193 recycle delay of 10 s were used, and 128 scans were accumulated. The spectral width
194 was 125 kHz. After the measurements, a spectrum of the rotor without sample has been
195 recorded and subtracted from the original spectrum to eliminate the broad signal
196 resulting from protons in the probehead and the rotor cap.

197 For ^{19}F MAS NMR experiments a Bruker 4 mm MAS NMR probe has been used.
198 300 scans were accumulated at a frequency of 376.46 MHz and rotation frequencies of
199 12.5 kHz. Single pulse duration was $2\ \mu\text{s}$, and a spectral width of 125 kHz and a recycle
200 delay of 10 s have been used. As external reference a liquid $\text{p-C}_6\text{H}_4\text{F}_2$ sample has been
201 measured, and the frequency with highest signal intensity has been set to -120 ppm with
202 respect to liquid CFCl_3 .

Revision #3

203 The $\{^1\text{H}\} \rightarrow ^{29}\text{Si}$ CPMAS NMR spectra were recorded at transmitter frequencies of
204 400.13 MHz and 79.49 MHz for ^1H and ^{29}Si , respectively. A standard 7mm Bruker
205 MAS NMR probe has been used at rotation frequencies of 4 kHz. The 90° pulse length
206 for ^1H was $7.6 \mu\text{s}$ ($\nu_{\text{rf}}(^1\text{H}) = \nu_{\text{rf}}(^{29}\text{Si}) = 33 \text{ kHz}$), and the recycle delay was 5 s. A total of
207 360 – 400 scans were accumulated, and tetramethylsilane was used as a reference for
208 both ^1H and ^{29}Si . For the CPMAS contact time dependent experiments contact times of
209 0.1 to 120 ms have been chosen. The $\{^1\text{H}\} \rightarrow ^{29}\text{Si}$ cross-depolarization MAS NMR
210 experiments (Kolodziejewski and Klinowski 2002; Wu et al. 1988) were carried out with a
211 contact-time of 10 ms, a dephase time of 5 ms for ^1H and 32 depolarization times
212 between $20 \mu\text{s}$ and 80 ms for ^{29}Si each totalling 1,200 scans.

213 The transmitter frequencies for the $\{^{19}\text{F}\} \rightarrow ^{29}\text{Si}$ CPMAS NMR experiments were
214 79.49 MHz and 376.45 MHz for ^{29}Si and ^{19}F , respectively. Sample spinning rate was
215 5.8 kHz in a standard 7 mm Bruker MAS probe. A total of 400 scans were accumulated.
216 Tetramethylsilane (TMS) and $p\text{-C}_6\text{H}_4\text{F}_2$ ($\delta = -120 \text{ ppm}$) have been used as reference for
217 ^{29}Si and ^{19}F , respectively. The 90° pulse length for ^{19}F was $5.6 \mu\text{s}$ ($\nu_{\text{rf}}(^{19}\text{F}) =$
218 $\nu_{\text{rf}}(^{29}\text{Si}) = 45 \text{ kHz}$), and a recycle delay of 5 s has been used. For the CPMAS contact-
219 time dependent experiments contact times of 0.1 to 120 ms have been chosen. The
220 $\{^{19}\text{F}\} \rightarrow ^{29}\text{Si}$ cross-depolarization MAS NMR experiments were carried with a contact-
221 time of 10 ms, a ^{19}F dephase time of 8 ms and 32 depolarization times between $20 \mu\text{s}$
222 and 80 ms for ^{29}Si totalling 3,200 scans each.

223 All MAS and CPMAS NMR spectra were fitted with mixed Gaussian / Lorentzian
224 lineshapes using the DmFit 2010 program (Massiot et al. 2002). Tolerances were

Revision #3

225 estimated by varying the line position and linewidth in the fit function observing χ^2
226 until a distinct change of χ^2 took place.

227

228 **RESULTS AND DISCUSSION**

229 **^{29}Si MAS NMR spectroscopy**

230 In order to clarify the influence of F on ordering of $\text{Si}/^{[4]}\text{Al}$ in the tetrahedral sheets of
231 phlogopite we compared ^{29}Si MAS NMR spectra of F-containing compositions to those
232 of pure hydroxyl-phlogopites (Fig. 1). Si has a tetrahedral coordination, being connected
233 through three bridging O atoms to three other tetrahedral sites which could be occupied
234 either by Al or Si. The fourth (non-bridging) O atom points to the octahedral sheet and
235 coordinates to Mg in phlogopite or Al in the Al-rich phlogopites. The four possible
236 signals at approximately -91, -87, -83 and -80 ppm can be assigned as $\text{Q}^3(\text{n Al})$ signals
237 with $\text{n} = 0\text{-}3$ (Fechtelkord et al. 2003a; Circone et al. 1991). An additional signal due to
238 an impurity phase has been found in the ^{29}Si MAS NMR spectra at about -94 to -95 ppm
239 for some of the samples. This has already been reported by Circone et al. (1991) who
240 suggested that it should result from some K-deficient clay-like layers in the phlogopites.
241 It could be also due to a talc component (Wunder and Melzer 2002) which cannot be
242 directly identified in the XRD patterns – it would only alter the cell dimensions of the
243 mica. The signal was only observed as a small shoulder but in some rare cases it showed
244 up to 10% relative signal intensity. The signal areas of the phlogopite signals correlate
245 with the relative amounts of those tetrahedral units in phlogopite, so that the $\text{Si}/^{[4]}\text{Al}$
246 ratio of the tetrahedral sheets can be easily determined by ^{29}Si MAS NMR from
247 equation 1 if Loewenstein's rule applies (Loewenstein 1954):

Revision #3

248
$$\frac{\text{Si}}{\text{IV Al}} = \frac{\sum_{n=0}^3 I(Q^3(nAl))}{\sum_{n=0}^3 \frac{n}{3} I(Q^3(nAl))} \quad (1)$$

249 Due to the fact that the real Si/Al ratio of the tetrahedral layers can now be determined,
250 it is possible to estimate the “real” x -value x_{est} in the stoichiometric phlogopite formula
251 $\text{K}(\text{Mg}_{3-x}\text{Al}_x)(\text{Al}_{1+x}\text{Si}_{3-x}\text{O}_{10})(\text{OH})_y\text{F}_{2-y}$ from equation 2.

252
$$x_{est} = \frac{3 - \frac{\text{Si}}{\text{IV Al}}}{1 + \frac{\text{Si}}{\text{IV Al}}} \quad (2)$$

253 The ^{29}Si MAS NMR data of Al-rich phlogopites with nominal composition
254 $\text{K}(\text{Mg}_{3-x}\text{Al}_x)(\text{Al}_{1+x}\text{Si}_{3-x}\text{O}_{10})(\text{OH})_y(\text{F})_{2-y}$ is listed in Table 1. The table contains signal
255 positions (δ), linewidths ($FWHM$) and areas of the signals. The spectra were fitted with
256 mixed Gaussian / Lorentzian lineshapes using the DmFit 2010 program (Massiot et al.
257 2002). Uncertainties were estimated by varying the line position and linewidth in the fit
258 function observing χ^2 until a distinct change of χ^2 took place. Total signal areas with
259 less than 100% are due to non-phlogopite ^{29}Si NMR signals from K-deficient clay
260 signal areas not listed here and mentioned above. The linewidth of all ^{29}Si NMR signals
261 ranges mostly around 2.6 – 2.8 ppm. The isotropic chemical shift of the signals shows a
262 dependence on the Al-content of the tetrahedral layers. An increasing Al-content leads
263 to a small shift of the ^{29}Si NMR signal to higher ppm-values. This can be attributed to
264 the change of the tetrahedral angle due to substitution of silicon by the larger Al.

Revision #3

265 Both the spectra and the calculation of the “real” Al-content x_{est} of the tetrahedral
266 sheets show a sharp decrease of the phlogopite’s ability to incorporate Al as F enters the
267 structure. The effect can be very well observed in Figure 2 where the estimated
268 octahedral Al content x_{est} is plotted as a function of the nominal Al-content of the oxide
269 gel x_{nom} . The estimated Al-content of the hydroxyl-phlogopites ($y = 2.0$) is always much
270 higher than that of F-containing samples of the same nominal Al-content. In contrast,
271 there is hardly any difference in the estimated Al-contents of samples of different F-
272 contents ($y = 1.2 - 1.8$). At low Al-contents the curves for different F-contents y are
273 approximately in the same range. However, for high values of nominal x the amount of
274 Al actually incorporated into the tetrahedral sheets is much higher for $y = 2.0$ than for
275 other compositions. This means that the mere presence of F in the mixture reduces the
276 ability to incorporate Al into the phlogopite structure drastically and has a stronger
277 influence than the exact ratio of OH/F.

278 At very high initial Al-contents a saturation effect can be observed: For $x_{nom} = 1.0$
279 and 1.2 the amount of Al incorporated is nearly the same ($x_{est} = 0.83$ for $y = 2.0$), for
280 $x_{nom} = 1.6$ it even decreases slightly. This indicates that for our synthesis conditions ($P =$
281 2 kbar, $T = 873$ K) the maximum amount of Al in the phlogopite structure has been
282 reached.

283

284

Revision #3

285 **¹H and ¹⁹F MAS NMR spectroscopy**

286 In the octahedral sheets, each OH position is surrounded by three cation sites which can
287 be occupied either by Mg or by Al. We therefore could expect four different
288 configurations of ions leading to four different signals in ¹H MAS NMR spectra:
289 Mg₃OH, Mg₂AlOH, MgAl₂OH, and Al₃OH. However, in a previous publication
290 (Langner et al. 2012) we showed that only two of these four signals, those for Mg₃OH
291 and the Mg₂AlOH, can be observed. Mg/Al is ordering in such a way that never two Al-
292 atoms occupy adjacent octahedral sites (Loewenstein's rule applying on octahedral
293 sites). The same is true for the ¹H MAS NMR spectra of F-containing phlogopites
294 shown in Figure 3. The resonance at 4.7 ppm is thought to be due to molecular water
295 which could be surface or defect water. It varies in all samples and its intensity shows
296 no relationship to the Al- or F-contents of the initial composition (see Fechtelkord et al.
297 2003a). Thus, the water resonance in Figure 3 is truncated for better visibility of the two
298 main hydroxyl signals at approximately 1.8 ppm and 0.6 ppm. The intensities of these
299 signals correlate directly with the Al-content of the octahedral sheets: when $x_{nom} = 0.0$,
300 only the signal at 0.6 ppm is observed. With increasing x_{nom} , the second signal at
301 1.8 ppm appears and increases in relative intensity. The two signals can thus be
302 assigned to the Mg₃OH (OH_{Mg}) and Mg₂AlOH (OH_{Al}) environments in the octahedral
303 sheets, respectively (Fechtelkord et al. 2003a). The ¹H MAS NMR data of Al-rich
304 phlogopites with nominal composition K (Mg_{3-x}Al_x) (Al_{1+x}Si_{3-x}O₁₀) (OH)_y (F)_{2-y} is listed
305 in Table 2. The table contains chemical shifts (δ), linewidths (*FWHM*) and areas of the
306 signals. The linewidth of both ¹H NMR signals is nearly constant around 1.0 – 1.4 ppm.
307 The chemical shift of the two signals shows a similar dependence on the Al-content as
308 that of the ²⁹Si MAS NMR signals. An increasing Al-content leads to a slight shift of

Revision #3

309 the ^1H NMR signal to higher ppm-values. The reason for that effect is very similar as
310 for the ^{29}Si NMR signal: the change of cation size from Mg to Al alters the bonding
311 angles of the OH-group to these cations.

312 Fechtelkord et al. (2003a) already demonstrated that OH-groups in the phlogopite
313 structure prefer coordination by two Mg and one Al (OH_{Al}) instead a coordination by
314 three Mg (OH_{Mg}). In contrast, F favors to be surrounded by Mg only. All experimental
315 values in Table 2 show higher $\text{OH}_{\text{Al}}/(\text{OH}_{\text{Al}}+\text{OH}_{\text{Mg}})$ ratios than predicted for a statistical
316 distribution. In the case of a statistical OH distribution inside the octahedral layers
317 $\text{OH}_{\text{Al}}/(\text{OH}_{\text{Al}}+\text{OH}_{\text{Mg}})$ should be equal to x_{est} . This implies a preferential occupation by
318 hydroxide ions of sites with Al as nearest neighbor which is in agreement with the
319 findings of Papin et al. (1997) from IR-spectroscopy.

320 The behaviors of ^1H MAS NMR signals of Al-rich phlogopites with different F-
321 contents support the findings made by ^{29}Si MAS NMR spectroscopy. As the hydroxyl
322 content increases, the $\text{OH}_{\text{Al}}/(\text{OH}_{\text{Al}}+\text{OH}_{\text{Mg}})$ ratio decreases because increasing the
323 number of OH groups per unit cell makes it progressively more difficult for them to
324 preferentially occupy only sites with Al coordinating them. However, similar to what
325 has been observed for the tetrahedral sheets in the ^{29}Si MAS NMR spectra, the Al-
326 content of samples with same x_{nom} increases with decreasing F-content.

327 The preference of OH for Al-containing sites and that of F for full Mg-containing
328 sites becomes visible when comparing the ^1H MAS NMR spectra to the ^{19}F MAS NMR
329 spectra of our phlogopite samples (Fig. 4). The ^{19}F MAS NMR spectra show two main
330 resonances at -150 ppm, and -173 ppm. Spinning sidebands of the main signals due to
331 the MAS technique are marked with asterisks. At low Al and F contents only the signal
332 at -173 ppm is observed (not shown in Fig. 4). With increasing Al-content the

Revision #3

333 component at -150 ppm appears and increases in relative intensity. At high F contents
334 ($y \leq 1.0$) and Al contents with $x \geq 0.1$ a third signal at -157 ppm appears. The first two
335 signals can be assigned to fluorine in phlogopite and are in agreement with the results of
336 Huve et al. (1992) who described the resonance at -173 ppm as Mg_3F units (F_{Mg}) and
337 the resonance at -150 ppm as Mg_2AlF (F_{Al}) units. They found a linear correlation
338 between the Al content of the sample and the intensity of the -150 ppm signal. The
339 signal at -157 ppm can be assigned to AlF_6 -units from the impurity phase potassium
340 aluminum hexafluoride ($\text{K}_3\text{AlF}_6 \cdot 0.5\text{H}_2\text{O}$). The signal position is characteristic for these
341 aluminum hexafluoride compounds (Harris and Jackson 1991). A fourth ^{19}F MAS NMR
342 signal from another minor F-containing impurity phase at approximately -176 ppm
343 (signal area is 3% and 9%) exists at compositions of $x_{\text{nom}} = 1.0, 1.2$ and $y = 1.6$. An
344 assignment of these broad and low intensity signals is difficult. The ^{19}F MAS NMR data
345 of Al-rich phlogopites with nominal composition
346 $\text{K}(\text{Mg}_{3-x}\text{Al}_x)(\text{Al}_{1+x}\text{Si}_{3-x}\text{O}_{10})(\text{OH})_y(\text{F})_{2-y}$ is listed in Table 3.

347 It can be observed that the intensity of the Mg_2AlF signal becomes stronger with
348 increasing Al-content of the octahedral layers which is very similar compared to the ^1H
349 MAS NMR signals. However, in the ^1H MAS NMR spectra the intensity of the
350 Mg_2AlOH signal is equal to or even higher than that of the Mg_3OH signal. In the ^{19}F
351 MAS NMR spectra the signal intensity corresponding to Mg_2AlF environments is
352 always much lower than the Mg_3F signal intensity which indicates that F prefers to be
353 co-ordinated by Mg only. As previously shown in Langner et al. (2012) Al is clustered
354 in both sheets. Therefore, it is possible that F and OH are also part of this clustering
355 with OH being located in the Al-rich parts of the structure and F favoring Mg- and Si-
356 rich environments.

Revision #3

357

358 $\{^1\text{H}\}/\{^{19}\text{F}\} \rightarrow ^{29}\text{Si}$ Cross polarization (CP) dynamics

359 In the cross polarization (CP) experiment the strong magnetic polarization of nuclei
360 with high natural abundance and high magnetogyric ratio such as ^1H or ^{19}F (the I
361 nucleus) is transferred to nuclei with low spectral sensitivity such as ^{29}Si via
362 heteronuclear dipolar interaction (the S nucleus). Contact time dependent $\{^1\text{H}\} \rightarrow ^{29}\text{Si}$
363 CPMAS NMR experiments have been carried out to yield direct information about
364 atomic site configurations (Pines et al. 1971; Pines et al. 1973). One of the contact time
365 dependent $\{^1\text{H}\} \rightarrow ^{29}\text{Si}$ CP MAS NMR intensity data experiments is shown in Figure 5.
366 The exponential increase of magnetization depends on the number of I spins and the
367 distance of these spins to the S nuclei. On the other hand the intensity curve decays
368 exponentially during excitation of the radio frequency pulse to approach
369 thermodynamical equilibrium for the occupancy of the energy levels with the lower B_I
370 field. The described model is called the “classical I-S model” (Kolodziejcki and
371 Klinowski 2002). The least-squares fit in Figure 5 using this model shows that it is too
372 simple to describe the experimental data.

373 In fact, a two stage rise as previously reported by Wu et al. (1988) can be observed.
374 In these cases the spin diffusion between I nuclei (the I^* nuclei) involved in the CP
375 transfer and other I nuclei not involved in the CP transfer is not sufficiently rapid and
376 produces an oscillatory CP transfer between I^* and S nuclei in stationary single crystals
377 (Müller et al. 1974). In polycrystalline material the oscillatory behavior sums up
378 because of angular distributions of the $I^* - S$ nuclei pairs. First, a very rapid increase in
379 the first tens of microseconds takes place related to heteronuclear spin-spin relaxation
380 (T_2) between I^* and S nuclei followed by a much slower increase due to spin diffusion

Revision #3

381 (T_{df}) between I and I^* nuclei. The ratio (λ) of both processes depends on the number of
382 protons n near the observed nucleus ($\lambda = 1/(n + I)$). However, in practice λ depends
383 also on group mobility. The whole cross-polarization can now be defined using the
384 following equation (Kolodziejski and Klinowski 2002)

$$385 \quad I(t) = I_0 e^{\left(\frac{t}{T_{1\rho}}\right)} \left[1 - \lambda e^{\left(\frac{t}{T_{df}}\right)} - (1 - \lambda) e^{\left(\frac{3t}{2T_{df}}\right)} e^{\left(\frac{t^2}{2T_2^2}\right)} \right] \quad (3)$$

386 The model can be described as I-I^{*}-S model. Two of the contact time dependent $\{^1\text{H}\}$
387 \rightarrow ^{29}Si CP MAS NMR intensity data experiments are shown in Figure 6. The solid lines
388 represent the least-squares fits of the data to equation 3. The data plotted as black
389 diamonds represents the same $\{^1\text{H}\} \rightarrow ^{29}\text{Si}$ CP MAS NMR intensity data as in Figure 5.
390 In contrast, now the least-squares fit using equation 3 describes the experimental data
391 very well.

392 In addition, depolarization experiments can help to estimate the proton spin diffusion
393 time (T_{df}), the spin-spin relaxation time (T_2) and the lambda parameter (λ), because here
394 there is no influence of the proton spin-lattice time in the rotating frame ($T_{1\rho}$). A
395 depolarization experiment is set up like a normal cross-polarization experiment. First
396 magnetization is transferred from the I spin reservoir to the S nuclei. While the S nuclei
397 magnetization is still locked in the transverse plane of the rotating frame, the proton
398 pulse is switched off leading to a dephasing of the I spins. Thus, turning on the proton
399 pulse again causes an inversion of magnetization transfer from the S nuclei to the proton
400 reservoir (Wu et al. 1988). The functional dependence of the signal intensity can be
401 described as

Revision #3

402
$$I(t) = I_0 \left[\lambda e^{\left(\frac{-t}{T_{df}}\right)} + (1-\lambda) e^{\left(\frac{-3t}{2T_{df}}\right)} e^{\left(\frac{-t^2}{2T_2^2}\right)} \right] \quad (4)$$

403 where t is the depolarization time. It is obvious that the functional behavior is
404 opposite to the CP experiment described in equation 3. In the first ten to hundred
405 microseconds there is a fast decrease in signal intensity due to heteronuclear I^*-S spin-
406 spin relaxation related to T_2 . Then there is a slower decrease due to $I-I^*$ spin-spin
407 diffusion related to T_{df} .

408 Figure 7 shows the results of the $\{^1\text{H}\} \rightarrow ^{29}\text{Si}$ CP-depolarization NMR experiments.
409 The signal intensity shows exactly the behavior described above. However, for longer
410 depolarization times the intensity decays with a time constant of $T_{1\rho}^* \sim T_{1\rho}(^1\text{H})$. For this
411 case equation 4 can be multiplied by a term $A \exp(-t/T_{1\rho}^*)$, where A is the amplitude
412 (Kolodziejski and Klinowski 2002). The parameters derived from the depolarization
413 experiments can then be applied as fit parameters for the cross-polarization experiments
414 using equation 3. All experimental data extracted from the $\{^1\text{H}\} \rightarrow ^{29}\text{Si}$ CP MAS NMR
415 and CP-depolarization NMR are listed in Table 4. The intensity $I(t)$ of the ^{29}Si signal for
416 a subsequent contact-time has been determined by regarding the maximum intensity
417 (i.e., signal height) of the Si-Si₂Al or the Si-SiAl₂ signal (depending on sample
418 composition) or the overall signal area of all Si-nAl signals. This method could be used
419 because in nearly all experiments the separate Q³(n Al) signals showed all the same
420 time constants. This means that the relative ratio of Q³(n Al) signal areas does not
421 change with increasing contact- or depolarization time. As an example the time
422 constants for the different Q³(n Al) NMR signals of one $\{^1\text{H}\} \rightarrow ^{29}\text{Si}$ CP MAS NMR
423 experiment are the same within uncertainty (Table 5) compared to the data of the area /
424 maximum fit used in Table 4.

Revision #3

425 The spin-spin relaxation times T_2 are longer than for hydrocarbons investigated with
426 $\{^1\text{H}\} \rightarrow ^{13}\text{C}$ CP MAS NMR investigations by Kolodziejski and Klinowski (2002) and
427 in the range of 290 – 530 μs (for ^{13}C approx. 10 – 100 μs). This can be attributed to the
428 longer H-Si distance in the phlogopite structure (C-H bond usually 1.1 Å) and a weaker
429 heteronuclear dipolar interaction. Tateyama et al. (1974) reported H-Si distances of
430 3.18 Å, 3.20 Å, and 3.22 Å for a hydroxyl-phlogopite. With increasing hydroxyl content
431 of the phlogopite ($y = 1.0$ to $y = 1.8$) T_2 decreases from 530 μs to 300 μs . The increased
432 density of protons leads to stronger heteronuclear dipolar interaction. The spin-diffusion
433 time T_{df} shows no clear correlation with the phlogopite composition. Compared to
434 proton spin diffusion in $\{^1\text{H}\} \rightarrow ^{13}\text{C}$ CP experiments (Kolodziejski and Klinowski
435 2002), the phlogopite proton spin diffusion is slow and in the range of tenths of
436 milliseconds (T_{df} in $\{^1\text{H}\} \rightarrow ^{13}\text{C}$ CP experiments is around 0.2 – 6 ms). The lambda
437 parameter ranges around $\lambda = 0.66 - 0.75$. λ is dependent on the number of protons n
438 contributing to the polarization ($\lambda = 1/(n + 1)$). The lambda ratio clearly decreases with
439 increasing hydroxyl content of the phlogopite. The proton spin-lattice time in the
440 rotating frame ($T_{1\rho}$) is very large and it is impossible to estimate them from the data.

441 In the same way as described for the $\{^1\text{H}\} \rightarrow ^{29}\text{Si}$ CPMAS and CP-depolarization
442 intensity data described above, $\{^{19}\text{F}\} \rightarrow ^{29}\text{Si}$ CPMAS and CP-depolarization intensity
443 data have been acquired. Figure 8 shows one of the $\{^{19}\text{F}\} \rightarrow ^{29}\text{Si}$ CP-depolarization
444 NMR experiments. The signal intensity shows the same behavior as for the $\{^1\text{H}\} \rightarrow ^{29}\text{Si}$
445 CP-depolarization experiment. Similar, for longer depolarization times the intensity
446 decays with a time constant of $T_{1\rho}^* \sim T_{1\rho}(^{19}\text{F})$ (Kolodziejski and Klinowski 2002).
447 Again, the parameters derived from the depolarization experiments can then be applied
448 as fit parameters for the cross-polarization experiments using equation 3. Results of two

Revision #3

449 of the contact time dependent $\{^{19}\text{F}\} \rightarrow ^{29}\text{Si}$ CP MAS NMR experiments are shown in
450 Figure 9. The solid lines represent the least-squares fits to equation 3. All experimental
451 data extracted from the $\{^{19}\text{F}\} \rightarrow ^{29}\text{Si}$ CP MAS NMR and CP-depolarization NMR are
452 listed in Table 6. The intensity $I(t)$ of the ^{29}Si signal for a subsequent contact-time has
453 been determined by regarding the maximum intensity (i.e., signal height) of the Si-Si₂Al
454 or the Si-SiAl₂ signal (depending on sample composition) or the overall signal area of
455 all Si-nAl signals. This is possible because the relative ratio of Q³(n Al) signal areas
456 does not change with increasing contact- or depolarization time (similar as for the
457 $\{^1\text{H}\} \rightarrow ^{29}\text{Si}$ CP MAS NMR experiments, see above).

458 Analyzing the data, the spin-spin relaxation times T_2 in the $\{^{19}\text{F}\} \rightarrow ^{29}\text{Si}$ CP MAS
459 NMR are longer than for the $\{^1\text{H}\} \rightarrow ^{29}\text{Si}$ CP MAS NMR experiments and are in the
460 range of 1 – 17 ms (290 – 530 μs for $\{^1\text{H}\} \rightarrow ^{29}\text{Si}$ CP MAS NMR). This can be
461 attributed to two facts. Firstly, the gyromagnetic ratio of ^{19}F is lower than for ^1H leading
462 to a weaker dipolar interaction. Secondly, the F-Si distance in the phlogopite structure is
463 longer because F substitutes OH. In structures of fluoro-phlogopites reported by Takeda
464 and Morosin (1975) and McCauley et al. (1973) this distance is much longer with 3.53 –
465 3.54 \AA compared to H-Si distances of 3.18 \AA , 3.20 \AA , and 3.22 \AA for a hydroxyl-
466 phlogopite reported by Tateyama et al. (1974). T_2 and the spin-diffusion time T_{df} show
467 no clear correlation with the phlogopite composition. T_{df} is very large for phlogopites
468 with high fluorine content but at lower F-content they are comparable to proton spin
469 diffusion times in the $\{^1\text{H}\} \rightarrow ^{29}\text{Si}$ CP MAS NMR experiments and are around 10 – 14
470 ms. The comparison of T_{df} and T_2 for the first two samples ($x_{nom} = 0.0, y = 0.5$ and x_{nom}
471 $= 0.3, y = 0.5$) in Table 6 compared to the other samples suggest that the Al-content has
472 also a large effect. However, x_{nom} reflects only the Al-content of the sol-gel. Comparing

Revision #3

473 the estimated Al-content x_{est} reveals that due to the fluorine content of the gel much less
474 Al is incorporated into the structure (compare x_{est} values in Table 6). Thus, an influence
475 of the Al-content on the CP dynamic parameters cannot be inferred. The lambda
476 parameter ranges around $\lambda = 0.75$. In contrast to the $\{^1\text{H}\} \rightarrow ^{29}\text{Si}$ CP MAS NMR
477 experiments where the proton spin-lattice time in the rotating frame ($T_{1\rho}$) is very large
478 and not possible to estimate, the $\{^{19}\text{F}\} \rightarrow ^{29}\text{Si}$ CP MAS NMR data shows a clear
479 decrease of intensity with larger contact times (Fig. 9). It ranges around 50 ms for
480 phlogopites at high fluorine contents and increases with decreasing fluorine content of
481 the phlogopite.

482 Summarizing it can be seen that the proton concentration clearly influences T_2 in the
483 $\{^1\text{H}\} \rightarrow ^{29}\text{Si}$ CPMAS NMR experiments while there is no similar trend regarding the
484 fluorine concentration in the $\{^{19}\text{F}\} \rightarrow ^{29}\text{Si}$ CP MAS NMR data. The lambda parameter
485 and the spin diffusion time T_{df} show no functional behavior in both cases. $T_{1\rho}$ is large in
486 the case for ^1H but shows for ^{19}F a clear dependence on the fluorine concentration
487 (lower values at higher fluorine concentration).

488

489 **$\{^1\text{H}\} \rightarrow ^{29}\text{Si}$ CPMAS NMR spectra**

490 If we keep in mind that the signal intensities of HO-Mg₃ and HO-Mg₂Al environments
491 in the ^1H MAS NMR spectra are very often equal or the HO-Mg₂Al signal is sometimes
492 higher than the HO-Mg₃ signal, the separation into clusters of original phlogopite
493 composition $(\text{K}(\text{Mg}_3)[\text{AlSi}_3\text{O}_{10}](\text{OH})_2)$ and clusters of ‘eastonite’ composition
494 $(\text{K}(\text{Mg}_2\text{Al})[\text{Al}_2\text{Si}_2\text{O}_{10}](\text{OH})_2)$ is not visible in one-dimensional $\{^1\text{H}\} \rightarrow ^{29}\text{Si}$ CPMAS
495 NMR spectra. Magnetization is transferred from both environments (HO-Mg₃ and HO-

Revision #3

496 Mg₂Al) to nearby silicons. Thus, the $\{^1\text{H}\} \rightarrow ^{29}\text{Si}$ CPMAS NMR spectrum shows a
497 superposition of the ^{29}Si signals of both phlogopite regions. This can be nicely seen in
498 Figure 10. The top spectrum shows the normal ^{29}Si MAS NMR spectrum for a
499 composition of $x_{nom} = 0.8$ and $y = 1.0$ (sample synthesized at 1073 K). The $\{^1\text{H}\} \rightarrow ^{29}\text{Si}$
500 CP MAS NMR spectra shown below the ^{29}Si MAS NMR spectrum have been recorded
501 using contact times of $t = 3, 5$ and 7 ms. Increasing contact time leads to farther
502 magnetization travel for the two spin-systems, and thus ^{29}Si nuclei at larger distances
503 from the hydrogen of the OH group can be reached. The CP MAS and the ^{29}Si MAS
504 NMR spectra look comparable: For the CPMAS NMR spectra, the estimated Al-content
505 x_{est}^* is between 0.38 and 0.41 while x_{est} obtained from the ^{29}Si MAS NMR spectrum is
506 0.37. x_{est}^* was calculated from the $\{^1\text{H}\} \rightarrow ^{29}\text{Si}$ CP MAS NMR signal intensities of the
507 Q³(nAl) signals similar as the ratio x_{est} from the ^{29}Si MAS NMR spectra using equations
508 1 and 2.

509 Differences are only visible in 2D $\{^1\text{H}\} \rightarrow ^{29}\text{Si}$ heteronuclear correlation (HETCOR)
510 CP MAS NMR spectroscopy which is an ideal tool to investigate the relationship
511 between ordering in the tetrahedral and octahedral sheets because it combines
512 information on the local ^1H environment in the octahedral sheet with that on tetrahedral
513 ^{29}Si environments nearby. These experiments were already carried out with the pure
514 hydroxyl phlogopites samples ($y = 2.0$, synthesis temperature $T = 873$ K) from the
515 present investigation in a previous study (Langner et al. 2012). It could be shown that
516 Al-rich Si environments in the tetrahedral sheet are more likely to be found in direct
517 neighborhood of Al-rich proton environments in the octahedral sheets. In contrast, the
518 ^{29}Si with a lower number of Al-atoms as next-nearest-neighbors are more often located
519 next to Al-free OH environments. As a result the structure is separated into clusters of

Revision #3

520 original phlogopite composition $(K(Mg_3)[AlSi_3O_{10}](OH)_2)$ and clusters of ‘eastonite’
521 composition $(K(Mg_2Al)[Al_2Si_2O_{10}](OH)_2)$ that encompass a whole T-O-T layer
522 package, although Al is presumed to be distributed in the phlogopite structure
523 homogeneously on a macroscopic level (Langner et al. 2012). The cluster size of the
524 mica substructures ‘phlogopite’ and ‘eastonite’ have been roughly estimated by
525 atomistic calculations given in Langner et al. (2012). The clusters are between 20 - 50 Å
526 in diameter. The size is too small to speak of two phases. However, they are large
527 enough for 2D $\{^1H\} \rightarrow ^{29}Si$ heteronuclear correlation (HETCOR) CP MAS NMR
528 spectroscopy to show the effect of Al-rich (‘eastonite’) and Al-poor (‘phlogopite’)
529 containing regions. The results can also be transferred on the results of the $\{^{19}F\} \rightarrow ^{29}Si$
530 CP MAS NMR spectra discussed below.

531 In addition, $\{^1H\} \rightarrow ^{27}Al$ 2D CP MAS (HETCOR) spectroscopy has already been
532 carried out in Fechtelkord et al. (2003b) on samples synthesized at 1073 K with high Al
533 contents ($x_{nom} = 0.8$) and F contents ($y = 0.5, 1.0$). The spectra show site connectivities
534 between the tetrahedral ^{27}Al signal and the two 1H NMR signals of HO- Mg_3 and HO-
535 Mg_2Al environments. The ^{27}Al octahedral signal is connected to the 1H signal of HO-
536 Mg_2Al environments only.

537

538

Revision #3

539 $\{^{19}\text{F}\} \rightarrow ^{29}\text{Si}$ CPMAS NMR spectra

540 The $\{^{19}\text{F}\} \rightarrow ^{29}\text{Si}$ CP MAS NMR spectra shown have been recorded using contact times
541 of $t = 3, 5$ and 7 ms. Increasing contact time leads to farther magnetization travel for the
542 two spin-systems, and thus ^{29}Si nuclei at larger distances from F can be reached. An
543 example of the three 1D $\{^{19}\text{F}\} \rightarrow ^{29}\text{Si}$ CP MAS NMR spectra of a phlogopite sample of
544 composition $x_{\text{nom}} = 0.7, y = 1.0$, is displayed in Figure 11. For comparison, the ^{29}Si MAS
545 NMR spectrum of the same sample [nominal composition $\text{K}(\text{Mg}_{2.3}\text{Al}_{0.7})(\text{Al}_{1.7}\text{Si}_{2.3}\text{O}_{10})$
546 (OH) F] is presented at the top. There is a large discrepancy between the CP MAS and
547 the ^{29}Si MAS NMR spectra: The Al-content of the octahedral sheet estimated from the
548 CPMAS NMR spectra, x_{est}^* , is always about 0.2 lower than that obtained from the ^{29}Si
549 MAS NMR spectra. x_{est}^* was calculated from the $\{^{19}\text{F}\} \rightarrow ^{29}\text{Si}$ CP MAS NMR $\text{Q}^3(\text{nAl})$
550 signal intensities in the same manner as the ratio x_{est} from the ^{29}Si MAS NMR spectra
551 using equations 1 and 2.

552 While the $\{^1\text{H}\} \rightarrow ^{29}\text{Si}$ CP MAS NMR spectra and ^{29}Si MAS NMR spectra showed
553 very often similar lineshapes for one sample, this seems to be completely different for
554 the $\{^{19}\text{F}\} \rightarrow ^{29}\text{Si}$ CP MAS NMR spectra. The fact that the relative intensity of the F-
555 Mg_2Al signal is always very low can be used to directly show a relationship between
556 octahedral F environments and tetrahedral Si environments. In 1D $\{^{19}\text{F}\} \rightarrow ^{29}\text{Si}$ CP
557 MAS NMR experiments, magnetization is transferred from the ^{19}F to the ^{29}Si nucleus,
558 and only those ^{29}Si nuclei that have ^{19}F nuclei nearby will contribute to the resulting CP
559 MAS NMR spectrum. If we assume that the amount of F being surrounded by Al can be
560 neglected, these 1D $\{^{19}\text{F}\} \rightarrow ^{29}\text{Si}$ CP MAS NMR spectra should reflect the local
561 composition and distribution of Si environments in the tetrahedral sheet next to F- and
562 Mg-rich clusters in the octahedral sheet.

Revision #3

563 It should be noted that the CPMAS NMR experiments are in principle
564 non-quantitative. However, as contact time dependent experiments show very long $T_{1\rho}$
565 times (as discussed below), the intensities depend greatly on the number and distance of
566 the fluorines near the silicon nuclei. This means that ^{29}Si nuclei close to F- and Mg-rich
567 octahedral environments have fewer tetrahedral Al atoms as next-nearest-neighbors than
568 the average over the whole structure. This lower value does not change much for spectra
569 recorded with different contact times which shows that this is not only true for Si-atoms
570 directly adjacent to the F-ion but also to some further in the structure. In many cases the
571 lower Al-content is also visible from a shift of the Si-nAl signal positions to more
572 shielded values. All this indicates that F is ordered in the Al-poor clusters of the
573 structure, consistent with the results for F-free compositions in a recent paper showing
574 the separation into clusters of Al-rich ('eastonite') and Al-poor ('phlogopite') containing
575 regions (Langner et al. 2012).

576 In addition, nearly all samples also showed a decrease in FWHM of the $\{^{19}\text{F}\} \rightarrow ^{29}\text{Si}$
577 CP MAS NMR signals compared to ^{29}Si MAS NMR signals. A comparison is given in
578 Table 7 containing the ^{29}Si MAS NMR data and Table 8 containing the $\{^{19}\text{F}\} \rightarrow ^{29}\text{Si}$ CP
579 MAS NMR data at a contact time of $t = 10$ ms. The ^{29}Si MAS NMR spectra contain
580 information on all the Si environments throughout the structure. Si-O-Al bond length
581 and bond angles slightly differ for Si-atoms in both types of clusters leading to broad
582 ^{29}Si MAS NMR signals. Signal widths in Table 7 are usually around 2.8 ppm. In
583 contrast, in $\{^{19}\text{F}\} \rightarrow ^{29}\text{Si}$ CPMAS NMR experiments only Si-atoms in one type of
584 cluster are considered. These environments are more homogeneous resulting in a smaller
585 signal width of approximately 2.1 ppm as shown in Table 8. High-power-decoupled
586 $\{^1\text{H}/^{19}\text{F}\} ^{29}\text{Si}$ MAS NMR experiments were carried out to check the dependence of ^{29}Si

Revision #3

587 signal linewidths on $^1\text{H}/^{19}\text{F} - ^{29}\text{Si}$ heteronuclear dipolar interaction. There was no
588 indication of broadening due to heteronuclear dipolar interaction (same lineshape with
589 and without decoupling).

590 Two-dimensional $\{^{19}\text{F}\} \rightarrow ^{27}\text{Al}$ 2D CPMAS (HETCOR) spectroscopy of fluorine-
591 and aluminum-rich phlogopites has been carried out in a previous study by Fechtelkord
592 et al. (2003b) on samples synthesized at 1073 K with high Al contents ($x_{\text{nom}} = 0.8$) and F
593 contents ($y = 0.5, 1.0$). It is not surprising that in comparison to the $\{^1\text{H}\} \rightarrow ^{27}\text{Al}$ 2D
594 CPMAS (HETCOR) spectrum there are no similar contributions from the Mg_3F and
595 Mg_2AlF sites to neighboring tetrahedral and octahedral Al sites in phlogopite. The
596 fluorine in the Mg_3F sites is only able to transfer magnetization to tetrahedral Al sites.
597 Magnetization transfer from fluorine to octahedral aluminum sites is not observed due
598 to the low abundance of Mg_2AlF sites.

599

600

ACKNOWLEDGMENTS

601 This work was financially supported by the European Science Foundation (ESF) under
602 the EUROCORES programme EuroMinSci (www.esf.org/eurominisci), through contact
603 No. ERAS-CT-2003-980409 of the European Commission, DG Research, FP6, and by
604 the Deutsche Forschungsgemeinschaft (DFG) under project No. Fe486/6-1. We thank
605 the associate editor Brian L. Phillips and two anonymous referees for their helpful
606 comments to improve the manuscript.

607

Revision #3

608

REFERENCES CITED

- 609 Baker, D.R. and Bossanyi, H. (1994) The combined effect of F and H₂O on
610 interdiffusion between peralkaline dacitic and rhyolitic melts. Contributions to
611 Mineralogy and Petrology, 117, 203-214.
- 612 Baker, D.R. and Vaillancourt, J. (1995) The low viscosities of F + H₂O-bearing granitic
613 melts and implications for melt extraction and transport. Earth and Planetary
614 Science Letters, 132, 199-211.
- 615 Berndt, J., Holtz, F., and Koepke, J. (2001) Experimental constraints on storage
616 conditions in the chemically zoned magma chamber of the Laacher See volcano.
617 Contributions to Mineralogy and Petrology, 140, 469-486.
- 618 Carroll, M.R. and Webster, J.D. (1994) Solubilities of sulphur, noble-gases, nitrogen,
619 chlorine, and fluorine in magmas. In: Carroll, M.R., Holloway, J.R. (Eds.),
620 Volatiles in Magmas, Reviews in Mineralogy and Geochemistry, 30, 231-279.
621 Mineralogical Society of America, Washington, D.C.
- 622 Christiansen, E.H., Burt, D.M., Sheridan, M.F., and Wilson, R.T. (1983) Petrogenesis of
623 topaz rhyolites from the Western United States. Contributions to Mineralogy and
624 Petrology, 83, 16-30.
- 625 Circone, S., Navrotsky, A., Kirkpatrick, R.J., and Graham, C.M. (1991) Substitution of
626 ^[6,4]Al in phlogopite: Mica characterization, unit-cell variation, ²⁷Al and ²⁹Si MAS-
627 NMR spectroscopy, and Al-Si distribution in the tetrahedral sheet. American
628 Mineralogist, 76, 1485-1501.
- 629 Dingwell, D.B., Scarfe, C.M., and Cronin, D.J. (1985) The effect of fluorine on
630 viscosities in the system Na₂O-Al₂O₃-SiO₂: implications for phonolites, trachytes
631 and rhyolites. American Mineralogist, 70, 80-87.

Revision #3

- 632 Dingwell, D.B., Knoche, R., and Webb, S.L. (1993) The effect of F on the density of
633 haplogranite melt. American Mineralogist, 78, 325-330.
- 634 Fechtelkord, M., Behrens, B., Holtz, F., Fyfe, C. A., Groat, L. A. and Raudsepp, M.
635 (2003a) Influence of F content on the composition of Al-rich synthetic phlogopite:
636 Part I. New information on structure and phase-formation from ^{29}Si , ^1H , and ^{19}F
637 MAS NMR spectroscopies. American Mineralogist, 88, 47-53.
- 638 Fechtelkord, M., Behrens, B., Holtz, F., Bretherton, J.L., Fyfe, C. A., Groat, L. A. and
639 Raudsepp, M. (2003b) Influence of F content on the composition of Al-rich
640 synthetic phlogopite: Part II. Probing the structural arrangement of aluminum in
641 tetrahedral and octahedral layers by ^{27}Al MQMAS and $^1\text{H}/^{19}\text{F}$ - ^{27}Al HETCOR and
642 REDOR experiments. American Mineralogist, 88, 1046-1057.
- 643 Foster, M.D. (1960) Interpretation of the composition of lithium micas. Geological
644 Survey Professional Paper, 354-E, 115-147.
- 645 Giordano, D., Romano, C., Dingwell, D.B., Poe, B., and Behrens, H. (2004) The
646 combined effects of water and fluorine on the viscosity of silicic magmas.
647 Geochimica et Cosmochimica Acta, 68, 5159-5168.
- 648 Hamilton, D.L. and Henderson, C.M.B. (1968) The preparation of silicate composition
649 by a gelling method. Mineralogical Magazine, 36, 832-838.
- 650 Harris, R.K. and Jackson, P. (1991) High-resolution fluorine-19 magnetic resonance of
651 solids. Chemical Reviews, 91, 1427-1440.
- 652 Huve, L., Delmotte, L., Martin, P., Le Dred, R., Baron, J., and Saehr, D. (1992) ^{19}F
653 MAS NMR study of structural fluorine in some natural and synthetic 2:1 layer
654 silicates. Clays and Clay Minerals, 40, 186-191.

Revision #3

- 655 Knoche, R., Dingwell, D.B., and Webb, S.L. (1995) Melt densities for leucogranites and
656 granitic pegmatites: partial molar volumes for SiO₂, Al₂O₃, Na₂O, K₂O, Li₂O,
657 Rb₂O, Cs₂O, MgO, CaO, SrO, BaO, B₂O₃, P₂O₅, F₂O, TiO₂, Nb₂O₅, Ta₂O₅, and
658 WO₃. *Geochimica et Cosmochimica Acta*, 59, 4645-4652.
- 659 Kolodziejwski, W. and Klinowski, J. (2002) Kinetics of Cross-Polarization in Solid-State
660 NMR: A Guide to Chemists. *Chemical Reviews*, 102, 613-628.
- 661 Langner, R., Fechtelkord, M., Garcia, A., Palin, E.J., and Lopez-Solano, J. (2012)
662 Aluminum ordering and clustering in Al-rich synthetic phlogopite: $\{^1\text{H}\} \rightarrow ^{29}\text{Si}$
663 CPMAS HETCOR spectroscopy and atomistic calculations. *American*
664 *Mineralogist*, 97, 341–352.
- 665 Loewenstein, W. (1954) The distribution of aluminum in the tetrahedra of silicates and
666 aluminates. *American Mineralogist*, 39, 92-96.
- 667 London, D. (1987) Internal differentiation of rare earth elements in pegmatites: effects
668 of boron, phosphorus and fluorine. *Geochimica et Cosmochimica Acta*, 51, 403-
669 420.
- 670 Manning, D.A.C. (1981) The effect of fluorine on liquidus phase relationships in the
671 system Qz-Ab-Or with excess water at 1 kb. *Contributions to Mineralogy and*
672 *Petrology*, 76, 206-215.
- 673 Massiot, D., Fayon, F., Capron, M., King, I., Le Calvé, S., Alonso, B., Durand, J.O.,
674 Bujoli, B., Gan, Z., and Hoatson, G. (2002) Modelling one- and two-dimensional
675 solid-state NMR spectra. *Magnetic Resonance in Chemistry*, 40, 70-76.
- 676 McCauley, J.W., Newnham, R.E., and Gibbs, G.V. (1973) Crystal-structure analysis of
677 synthetic fluorophlogopite. *American Mineralogist*, 58, 249-254.

Revision #3

- 678 Müller, L., Kumar, A., Baumann, T., and Ernst, R.R. (1974) Transient Oscillations in
679 NMR Cross-Polarization Experiments in Solids. *Physical Review Letters*, 32, 1402-
680 1406.
- 681 Papin, A., Sergent, J., and Robert, J.-L. (1997) Intersite OH-F distribution in an Al-rich
682 phlogopite. *European Journal of Mineralogy*, 9, 501-508.
- 683 Pichavant, M. and Manning, D.A.C. (1984) Petrogenesis of tourmaline granites and
684 topaz granites; the contribution of experimental data. *Physics of Earth Planetary*
685 *Interiors*, 35, 31-50.
- 686 Pines, A., Gibby, M.G., and Waugh, J.S. (1971) Proton-enhanced nuclear induction
687 spectroscopy. A method for high resolution NMR of dilute spins in solids. *Journal*
688 *of Chemical Physics*, 56, 1776-1777.
- 689 Pines, A., Gibby, M.G., and Waugh, J.S. (1973) Proton-enhanced NMR of dilute spins
690 in solids. *Journal of Chemical Physics*, 59, 569-590.
- 691 Slichter, C.P. (1990) *Principles of Magnetic Resonance*. 3rd edition, Springer-Verlag,
692 Heidelberg.
- 693 Takeda, H. and Morosin, B. (1975) Comparison of observed and predicted structural
694 parameters of mica at high-temperature. *Acta Crystallographica B*, 31, 2444-2452.
- 695 Tateyama, H., Shimoda, S., and Sudo, T. (1974) The crystal structure of synthetic
696 Mg(IV) mica. *Zeitschrift für Kristallographie, Kristallgeometrie, Kristallphysik und*
697 *Kristallchemie*, 139, 196-206.
- 698 Webster, J.D., Holloway, J.R., and Hervig, R.L. (1987) Phase equilibria of a Be, U and
699 F-enriched vitrophyre from Spor Mountain, Utah. *Geochimica et Cosmochimica*
700 *Acta*, 51, 389-402.

Revision #3

- 701 Weidner, J.R. and Martin, R.F. (1987) Phase equilibria of a F-rich leucogranite from the
702 St. Austell pluton, Cornwall. *Geochimica et Cosmochimica Acta*, 51, 1591-1597.
- 703 Whalen, J.B., Currie, K.L., and Chappell, B.W. (1987) A-type granites: geochemical
704 characteristics, discrimination, and petrogenesis. *Contributions to Mineralogy and
705 Petrology*, 95, 407-419.
- 706 Wu, X., Zhang, S., and Wu, X. (1988) Two-stage feature of Hartmann-Hahn cross
707 relaxation in magic-angle spinning. *Physical Review B*, 37, 9827-9829.
- 708
- 709
- 710

Revision #3

FIGURE CAPTIONS

711

712

713 **Figure 1** Comparison of ^{29}Si MAS NMR spectra of phlogopites with nominal
714 composition $\text{K}(\text{Mg}_{3-x}\text{Al}_x)(\text{Al}_{1+x}\text{Si}_{3-x}\text{O}_{10})(\text{OH})_y\text{F}_{2-y}$ with different Al- and F-contents.
715 The Al-content of the tetrahedral sheets calculated from the relative signal intensities,
716 x_{est} (calculated from eq. 1 and 2), for each spectrum is given in the figure.

717 **Figure 2** Plot of the experimentally derived (additional) Al-content of tetrahedral sheets
718 x_{est} (calculated from eq. 1 and 2) of the phlogopites against the Al-content of the initial
719 gel mixture x_{nom} . The black line indicates a complete reaction of the starting material to
720 phlogopite ($x_{est} = x_{nom}$).

721 **Figure 3** Comparison of ^1H MAS NMR spectra of OH- and Al-rich phlogopites with
722 nominal composition $\text{K}(\text{Mg}_{3-x}\text{Al}_x)(\text{Al}_{1+x}\text{Si}_{3-x}\text{O}_{10})(\text{OH})_y\text{F}_{2-y}$. The ratio $\text{I}[\text{H-OMg}_2\text{Al}]/$
723 $(\text{I}[\text{H-OMg}_2\text{Al}] + \text{I}[\text{H-OMg}_3])$ for each spectrum is given in the figure, abbreviated as
724 ‘Al/(Mg+Al)’. The water resonance at 4.7 ppm is cut off for a better visibility of the two
725 main signals.

726 **Figure 4** Comparison of ^{19}F MAS NMR spectra of OH- and Al-rich phlogopites with
727 nominal composition $\text{K}(\text{Mg}_{3-x}\text{Al}_x)(\text{Al}_{1+x}\text{Si}_{3-x}\text{O}_{10})(\text{OH})_y\text{F}_{2-y}$. The ratio
728 $\text{I}[\text{F-Mg}_2\text{Al}]/(\text{I}[\text{F-Mg}_2\text{Al}] + \text{I}[\text{F-Mg}_3])$ is given below the spectra, abbreviated as
729 ‘Al/(Mg+Al)’. Spinning sidebands are marked by asterisks.

730 **Figure 5** Experimental CP magnetization data derived from contact-time dependent
731 $\{^1\text{H}\} \rightarrow ^{29}\text{Si}$ CP-MAS NMR experiments for phlogopites with nominal composition
732 $\text{K}(\text{Mg}_{3-x}\text{Al}_x)(\text{Al}_{1+x}\text{Si}_{3-x}\text{O}_{10})(\text{OH})_y\text{F}_{2-y}$ with $x_{nom} = 0.5$, $y = 1.0$ (*black diamonds*). The
733 solid lines represent the least-squares fits using the ‘classical I-S model’ (Kolodziejki
734 and Klinowski 2002).

Revision #3

735 **Figure 6** Experimental CP magnetization data derived from contact-time dependent
736 $\{^1\text{H}\} \rightarrow ^{29}\text{Si}$ CP-MAS NMR experiments for phlogopites with nominal composition
737 $\text{K}(\text{Mg}_{3-x}\text{Al}_x)(\text{Al}_{1+x}\text{Si}_{3-x}\text{O}_{10})(\text{OH})_y\text{F}_{2-y}$ with $x_{nom} = 0.8$, $y = 1.8$ (*open circles*) and $x_{nom} =$
738 0.5 , $y = 1.0$ (*black diamonds*). The solid lines represent the least-squares fits of the data
739 to equation 3.

740 **Figure 7** Experimental depolarization data derived from $\{^1\text{H}\} \rightarrow ^{29}\text{Si}$ CP-depolarization
741 NMR experiments for phlogopites with nominal composition
742 $\text{K}(\text{Mg}_{3-x}\text{Al}_x)(\text{Al}_{1+x}\text{Si}_{3-x}\text{O}_{10})(\text{OH})_y\text{F}_{2-y}$ with $x_{nom} = 0.8$ and $y = 1.8$. The solid line
743 represents the least-squares fit of the data to equation 4.

744 **Figure 8** Experimental depolarization data derived from $\{^{19}\text{F}\} \rightarrow ^{29}\text{Si}$ CP-
745 depolarization NMR experiments for phlogopites with nominal composition
746 $\text{K}(\text{Mg}_{3-x}\text{Al}_x)(\text{Al}_{1+x}\text{Si}_{3-x}\text{O}_{10})(\text{OH})_y\text{F}_{2-y}$ with $x_{nom} = 0.3$ and $y = 0.5$. The solid line
747 represents the least-squares fit of the data to equation 4.

748 **Figure 9** Experimental CP magnetization data derived from contact-time dependent
749 $\{^{19}\text{F}\} \rightarrow ^{29}\text{Si}$ CP-MAS NMR experiments for phlogopites with nominal composition
750 $\text{K}(\text{Mg}_{3-x}\text{Al}_x)(\text{Al}_{1+x}\text{Si}_{3-x}\text{O}_{10})(\text{OH})_y\text{F}_{2-y}$ with $x_{nom} = 0.0$, $y = 0.5$ (*open circles*) and $x_{nom} =$
751 0.3 , $y = 0.5$ (*black diamonds*). The solid lines represent the least-squares fits of the data
752 to equation 3.

753 **Figure 10** 1D $\{^1\text{H}\} \rightarrow ^{29}\text{Si}$ CPMAS NMR spectra of the sample with nominal
754 composition $x_{nom} = 0.8$, $y = 1.0$ (synthesized at 1073 K), recorded at contact times of $t =$
755 3, 5, and 7 ms, respectively. For comparison, the ^{29}Si MAS NMR spectrum of the same
756 sample is also shown (top). x_{est}^* was calculated from the $\{^1\text{H}\} \rightarrow ^{29}\text{Si}$ CP MAS NMR
757 signal intensities of the $\text{Q}^3(\text{nAl})$ signals similar as the ratio x_{est} from the ^{29}Si MAS NMR
758 spectra using equations 1 and 2.

Revision #3

759 **Figure 11** 1D $\{^{19}\text{F}\} \rightarrow ^{29}\text{Si}$ CPMAS NMR spectra of the sample with nominal
760 composition $x_{nom} = 0.7$, $y = 1.0$ (synthesized at 873 K), recorded at contact times of $t =$
761 3, 5, and 7 ms, respectively. For comparison, the ^{29}Si MAS NMR spectrum of the same
762 sample is also shown (top). x_{est}^* was calculated from the $\{^{19}\text{F}\} \rightarrow ^{29}\text{Si}$ CP MAS NMR
763 signal intensities of the $\text{Q}^3(\text{nAl})$ signals similar as the ratio x_{est} from the ^{29}Si MAS NMR
764 spectra using equations 1 and 2.
765

Revision #3

766 Table 1. ²⁹Si MAS NMR data of Al-rich phlogopites with nominal composition
 767 K(Mg_{3-x}Al_x)(Al_{1+x}Si_{3-x}O₁₀)(OH)_y(F)_{2-y}. The table contains chemical shifts (δ), linewidths (FWHM) and areas
 768 of the signals. x_{est} was calculated from equation 1 and 2. Total signal areas with less than 100% are due to
 769 non-phlogopite ²⁹Si NMR signals from K-deficient clay signal areas not listed here.

x _{nom}	y	x _{est}	Q ³ (3Al)			Q ³ (2Al)			Q ³ (1Al)			Q ³ (0Al)		
			δ [ppm]	FWHM [ppm]	Area [%]	δ [ppm]	FWHM [ppm]	Area [%]	δ [ppm]	FWHM [ppm]	Area [%]	δ [ppm]	FWHM [ppm]	Area [%]
0.1	1.2	0.04				-84.1	2.8	25	-88.2	2.6	56	-92.3	2.8	19
0.2	1.2	0.11				-84.7	2.9	31	-88.5	2.4	53	-92.5	2.9	16
0.3	1.2	0.17	-80.4	2.8	5	-83.9	2.6	29	-87.7	2.7	44	-91.4	2.8	16
0.4	1.2	0.14	-80.0	2.7	3	-83.9	2.8	29	-87.8	2.7	45	-91.3	2.8	17
0.5	1.2	0.24	-79.9	2.8	9	-83.8	2.6	30	-87.7	2.7	42	-91.3	2.8	15
0.6	1.2	0.23	-79.9	2.8	8	-83.8	2.7	30	-87.7	2.7	40	-91.3	2.8	15
0.7	1.2	0.35	-80.1	2.6	10	-83.9	2.6	40	-87.6	2.6	43	-91.3	2.1	7
0.1	1.6	0.05	-79.6	2.8	3	-83.5	2.7	20	-87.4	2.6	46	-91.0	2.8	20
0.2	1.6	0.03				-83.6	2.6	24	-87.6	2.7	52	-91.2	2.8	20
0.3	1.6	0.08				-84.0	2.6	27	87.8	2.7	51	-91.4	2.8	17
0.4	1.6	0.10	-80.0	2.8	4	-83.7	2.7	25	-87.4	2.7	40	-90.2	2.8	21
0.5	1.6	0.35	-79.6	2.9	13	-83.3	2.6	38	-87.0	2.7	38	-90.7	2.8	11
0.6	1.6	0.28	-79.8	2.8	8	-83.5	2.3	35	-87.3	2.5	47	-91.2	2.8	10
0.8	1.6	0.36	-80.1	2.8	12	-83.7	2.7	40	-87.4	2.7	38	-91.3	2.8	10
1.0	1.6	0.63	-80.1	1.9	39	-83.7	2.4	34	-87.2	2.8	21	-91.1	2.9	6
1.2	1.6	0.66	-80.0	1.8	40	-83.6	2.6	38	-87.3	2.8	16	-90.7	2.9	6
0.2	1.8	0.14	-79.0	2.8	3	-82.8	2.6	27	-86.8	2.8	50	-90.3	2.8	14
0.3	1.8	0.17	-79.7	2.7	4	-83.2	2.4	33	-86.8	2.6	44	-90.3	2.8	17
0.5	1.8	0.26	-80.3	2.8	8	-83.5	2.6	35	-87.3	2.7	44	-90.5	2.8	13
0.6	1.8	0.46	-79.5	2.3	17	-83.0	2.4	43	-86.6	2.4	35	-90.2	2.1	5
1.2	1.8	0.71	-79.4	1.7	50	-83.0	2.4	30	-86.7	2.8	14	-90.2	2.9	6
1.6	1.8	0.67	-79.4	1.8	43	-82.8	2.5	36	-86.1	2.8	14	-89.6	2.9	7
0.4	2.0	0.25	-80.1	2.8	7	-83.7	2.6	34	-87.6	2.7	43	-90.8	2.8	13
0.5	2.0	0.29	-79.8	2.9	10	-83.1	2.7	34	-87.1	2.9	37	-90.9	2.9	14
0.8	2.0	0.67	-79.4	2.3	42	-82.8	2.5	36	-86.3	2.7	17	-89.8	2.4	5
1.0	2.0	0.83	-79.4	1.4	61	-82.6	2.5	31	-86.2	2.0	8			
1.2	2.0	0.87	-79.6	1.3	72	-82.8	2.6	20	-86.7	2.6	8			
1.6	2.0	0.65	-79.4	2.0	36	-82.9	2.6	42	-86.6	2.7	19	-90.0	2.9	3

Note: Error ranges are as follows: x_{est} ± 0.10, δ ± 0.3 ppm, FWHM ± 0.4 ppm, area ± 3%

770
771

Revision #3

772 Table 2. ^1H MAS NMR data of Al-rich phlogopites with nominal composition
 773 $\text{K}(\text{Mg}_{3-x}\text{Al}_x)(\text{Al}_{1+x}\text{Si}_{3-x}\text{O}_{10})(\text{OH})_y(\text{F})_{2-y}$. The table contains chemical shifts (δ), linewidths (FWHM) and areas
 774 of the signals. x_{est} was calculated from equation 1 and 2.

x_{nom}	y	x_{est}	$\text{Mg}_3\text{OH} (\text{OH}_{\text{Mg}})$			$\text{Mg}_2\text{AlOH} (\text{OH}_{\text{Al}})$			$\frac{\text{OH}_{\text{Al}}}{(\text{OH}_{\text{Al}} + \text{OH}_{\text{Mg}})}$
			δ [ppm]	FWHM [ppm]	Area [%]	δ [ppm]	FWHM [ppm]	Area [%]	
0.8	1.6	0.36	0.6	1.0	46	1.8	1.3	54	0.54
1.0	1.6	0.63	1.5	1.0	34	2.8	1.4	66	0.66
1.2	1.6	0.66	1.1	1.2	29	2.4	1.2	71	0.71
1.2	1.8	0.71	1.0	1.0	26	2.3	1.2	74	0.74
1.6	1.8	0.67	1.0	0.9	20	2.3	1.3	80	0.80
0.8	2.0	0.67	1.5	1.8	35	3.0	1.8	65	0.65
1.0	2.0	0.83	1.9	1.1	22	3.2	1.1	78	0.78
1.2	2.0	0.87	1.3	1.2	19	2.5	1.0	81	0.81
1.6	2.0	0.65	1.7	1.1	32	3.0	1.3	68	0.68

Note: Error ranges are as follows: $x_{\text{est}} \pm 0.10$, $\delta \pm 0.1$ ppm, FWHM ± 0.2 ppm, area $\pm 3\%$

775
776

Revision #3

777 Table 3. ¹⁹F MAS NMR data of Al-rich phlogopites with nominal composition
 778 K (Mg_{3-x}Al_x) (Al_{1+x}Si_{3-x}O₁₀) (OH)_y (F)_{2-y}. The table contains chemical shifts (δ), linewidths (FWHM) and areas
 779 of the signals. x_{est} was calculated related to equation 1 and 2.

x _{nom}	y	x _{est}	Mg ₃ F (F _{Mg})			Mg ₂ AlF (F _{Mg})			$\frac{F_{Al}}{(F_{Al} + F_{Mg})}$	K ₃ AlF ₆ *0.5 H ₂ O			Other phases
			δ [ppm]	FWHM [ppm]	Area [%]	δ [ppm]	FWHM [ppm]	Area [%]		δ [ppm]	FWHM [ppm]	Area [%]	
0.8	1.6	0.36	-173.3	3.5	88	-149.3	3.7	12	0.12				
1.0	1.6	0.63	-172.9	3.6	81	-149.1	3.5	16	0.16				3
1.2	1.6	0.66	-172.2	3.4	28	-147.8	1.7	5	0.16				9
			-175.5	3.0	50	-150.0	2.8	8					
1.2	1.8	0.71	-173.3	3.5	81	-149.3	4.0	10	0.11	-157.8	2.5	9	
1.6	1.8	0.67	-171.0	3.5	50	-147.4	3.2	19	0.28	-157.4	2.5	31	

Note: Error ranges are as follows: x_{est} ± 0.10. δ ± 0.5 ppm. FWHM ± 0.3 ppm. area ± 3%; * unidentified

780

781

782

783

Revision #3

784 Table 4. $\{^1\text{H}\} \rightarrow ^{29}\text{Si}$ CP MAS NMR data of Al-rich phlogopites with nominal composition
 785 $\text{K}(\text{Mg}_{3-x}\text{Al}_x)(\text{Al}_{1+x}\text{Si}_{3-x}\text{O}_{10})(\text{OH})_y(\text{F})_{2-y}$ and synthesis temperature T according to the I-I*-S Model. The spin-
 786 spin relaxation time (T_2), the ^1H spin-diffusion time (T_{df}), the ^1H spin-relaxation time in the rotating frame
 787 ($T_{1\rho}$) and the lambda factor (λ) were calculated from cross-polarization experiments according to equation 3
 788 and depolarization experiments according to equation 4.

x_{nom}	y	x_{est}	T [K]	T_2 [μs]	T_{df} [ms]	$T_{1\rho}$ [s]	λ
0.4	1.0	0.25	1073	526 ± 30	10 ± 1	n.a.	0.78 ± 0.05
0.5	1.0	0.29	1073	517 ± 50	12 ± 1	n.a.	0.76 ± 0.02
0.6	1.0	0.29	1073	495 ± 50	15 ± 1	n.a.	0.71 ± 0.02
0.7	1.0	0.37	1073	382 ± 50	9 ± 2	n.a.	0.83 ± 0.02
0.8	1.0	0.37	1073	457 ± 60	14 ± 1	n.a.	0.79 ± 0.01
0.4	1.5	0.25	1073	372 ± 12	17 ± 1	n.a.	0.66 ± 0.01
0.6	1.5	0.35	1073	307 ± 8	12 ± 1	n.a.	0.68 ± 0.01
0.8	1.8	0.50	1073	292 ± 12	12 ± 1	n.a.	0.67 ± 0.01
0.5	1.6	0.35	873	378 ± 15	8 ± 2	n.a.	0.68 ± 0.01
0.7	1.8	0.46	873	350 ± 6	11 ± 1	n.a.	0.70 ± 0.01

Note: n.a.: Value cannot be estimated

789
790

Revision #3

791 Table 5. $\{^1\text{H}\} \rightarrow ^{29}\text{Si}$ CP MAS NMR data of Al-rich phlogopites with nominal composition
792 $\text{K}(\text{Mg}_{3-x}\text{Al}_x)(\text{Al}_{1+x}\text{Si}_{3-x}\text{O}_{10})(\text{OH})_y(\text{F})_{2-y}$ with $x = 0.5$ and $y = 1.6$ according to the I-I*-S Model for the different
793 ^{29}Si NMR signals. The spin-spin relaxation time (T_2), the ^1H spin-diffusion time (T_{df}), the ^1H spin-relaxation
794 time in the rotating frame ($T_{1\rho}$) and the lambda factor (λ) were calculated from cross-polarization
795 experiments according to equation 3 and depolarization experiments according to equation 4.

^{29}Si Signal	T_2 [μs]	T_{df} [ms]	$T_{1\rho}$ [s]	λ
$\text{Q}^3(3\text{Al})$	323 ± 12	11 ± 1	n.a.	0.68 ± 0.02
$\text{Q}^3(2\text{Al})$	312 ± 12	11 ± 1	n.a.	0.67 ± 0.02
$\text{Q}^3(1\text{Al})$	352 ± 11	12 ± 1	n.a.	0.75 ± 0.05
$\text{Q}^3(0\text{Al})$	301 ± 25	12 ± 4	n.a.	0.57 ± 0.08

Note: n.a.: Value cannot be estimated

796
797

Revision #3

798 Table 6. $\{^{19}\text{F}\} \rightarrow ^{29}\text{Si}$ CP MAS NMR data of Al-rich phlogopites with nominal composition
799 $\text{K}(\text{Mg}_{3-x}\text{Al}_x)(\text{Al}_{1+x}\text{Si}_{3-x}\text{O}_{10})(\text{OH})_y(\text{F})_{2-y}$, according to the I-S Model. The spin-spin relaxation time (T_2), the
800 ^1H spin-diffusion time (T_{df}), the ^1H spin-relaxation time in the rotating frame ($T_{1\rho}$) and the lambda factor (λ)
801 were calculated from cross-polarization experiments according to equation 3 and depolarization
802 experiments according to equation 4.

x_{nom}	y	x_{est}	T [K]	T_2 [ms]	T_{df} [ms]	$T_{1\rho}$ [ms]	λ
0.1	0.2	0.01	873	17 ± 1	222 ± 12	56 ± 1	0.76 ± 0.01
0.0	0.5	0.01	873	22 ± 2	162 ± 12	47 ± 2	0.76 ± 0.01
0.3	0.5	0.08	873	2.2 ± 0.2	9 ± 1	1780 ± 110	0.71 ± 0.03
0.6	0.5	0.33	873	12 ± 5	10 ± 1	385 ± 78	0.63 ± 0.01
0.8	0.8	0.41	873	1.4 ± 0.5	10 ± 2	n.a.	0.86 ± 0.01
0.7	1.0	0.51	873	1.2 ± 0.5	14 ± 1	n.a.	0.81 ± 0.02

Note: n.a.: Value cannot be estimated

803

804

805

Revision #3

806 Table 7. ^{29}Si MAS NMR data of Al-rich phlogopites with nominal composition
 807 $\text{K}(\text{Mg}_{3-x}\text{Al}_x)(\text{Al}_{1+x}\text{Si}_{3-x}\text{O}_{10})(\text{OH})_y(\text{F})_{2-y}$. The table contains chemical shifts (δ), linewidths (FWHM) and areas
 808 of the signals. x_{est} was calculated related to equation 1 and 2. Total signal areas with less than 100% are
 809 due to non-phlogopite ^{29}Si NMR signals from K-deficient clay signal areas not listed here.

x_{nom}	y	x_{est}	$\text{Q}^3(3\text{Al})$			$\text{Q}^3(2\text{Al})$			$\text{Q}^3(1\text{Al})$			$\text{Q}^3(0\text{Al})$		
			δ [ppm]	FWHM [ppm]	Area [%]	δ [ppm]	FWHM [ppm]	Area [%]	δ [ppm]	FWHM [ppm]	Area [%]	δ [ppm]	FWHM [ppm]	Area [%]
0.1	0.2	0.01				-85.1	2.5	22	-88.9	2.4	58	-93.1	2.8	20
0.0	0.5	0.01				-84.7	2.2	20	-88.4	1.9	61	-92.4	2.0	19
0.3	0.5	0.08				-84.2	2.7	27	-88.2	2.7	54	91.8	2.8	16
0.6	0.5	0.33	-80.7	2.8	10	-83.5	2.6	39	-86.9	2.7	41	-90.6	2.8	10
0.8	0.8	0.41	-80.2	2.8	13	-83.8	2.6	44	-87.4	2.5	36	-91.0	2.8	7
0.7	1.0	0.51	-79.9	2.6	23	-83.6	2.5	43	-87.2	2.5	27	90.7	2.8	7

Note: Error ranges are as follows: $x_{\text{est}} \pm 0.10$, $\delta \pm 0.3$ ppm, FWHM ± 0.4 ppm, area $\pm 3\%$

810

811 Table 8. $\{^{19}\text{F}\} \rightarrow ^{29}\text{Si}$ CP MAS NMR data of Al-rich phlogopites with nominal composition
 812 $\text{K}(\text{Mg}_{3-x}\text{Al}_x)(\text{Al}_{1+x}\text{Si}_{3-x}\text{O}_{10})(\text{OH})_y(\text{F})_{2-y}$ at a contact time of $t = 10$ ms. The table contains chemical shifts (δ),
 813 linewidths (FWHM) and areas of the signals. x_{est}^* was calculated from the $\{^{19}\text{F}\} \rightarrow ^{29}\text{Si}$ CP MAS NMR signal
 814 intensities of the $\text{Q}^3(\text{n Al})$ signals related to equation 1 and 2.

x_{nom}	y	x_{est}^*	$\text{Q}^3(3\text{Al})$			$\text{Q}^3(2\text{Al})$			$\text{Q}^3(1\text{Al})$			$\text{Q}^3(0\text{Al})$		
			δ [ppm]	FWHM [ppm]	Area [%]	δ [ppm]	FWHM [ppm]	Area [%]	δ [ppm]	FWHM [ppm]	Area [%]	δ [ppm]	FWHM [ppm]	Area [%]
0.1	0.2	-0.08				-84.6	1.9	17	-88.2	2.3	56	-92.2	3.0	27
0.0	0.5	-0.02				-85.4	2.2	19	-88.9	2.0	59	-92.7	2.2	22
0.3	0.5	0.06				-84.6	2.1	21	-88.3	2.4	66	-92.2	2.2	13
0.6	0.5	0.34	-80.7	1.5	2	-84.3	2.9	49	-87.9	2.5	47	-91.9	1.0	2
0.8	0.8	0.38	-80.7	2.0	5	-84.6	2.6	51	-88.0	2.3	41	-92.4	0.9	3
0.7	1.0	0.38	-80.8	2.0	7	-84.6	3.1	51	-88.1	2.4	35	-92.1	1.9	7

Note: Error ranges are as follows: $x_{\text{est}} \pm 0.10$, $\delta \pm 0.3$ ppm, FWHM ± 0.4 ppm, area $\pm 3\%$

815

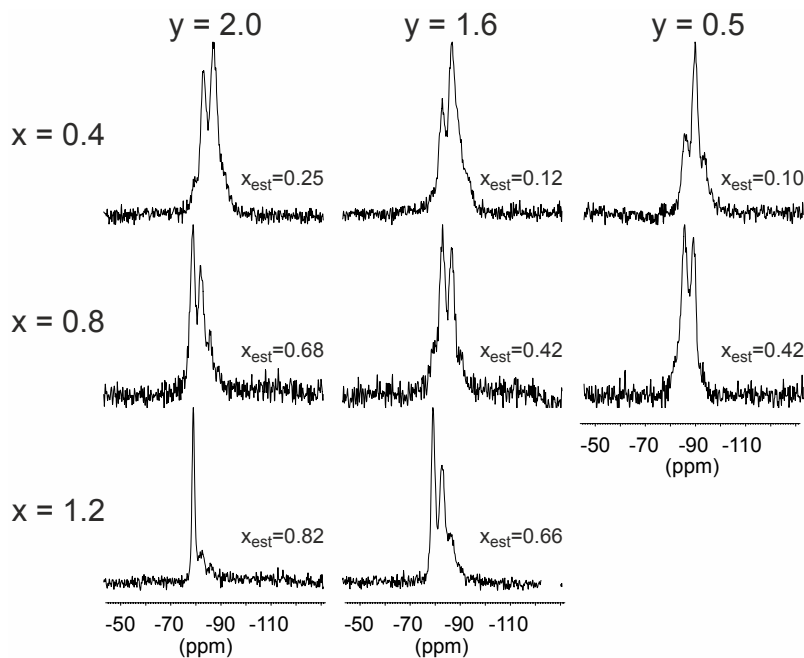
816

817

818

Revision #3

819 Figure 1
820



821

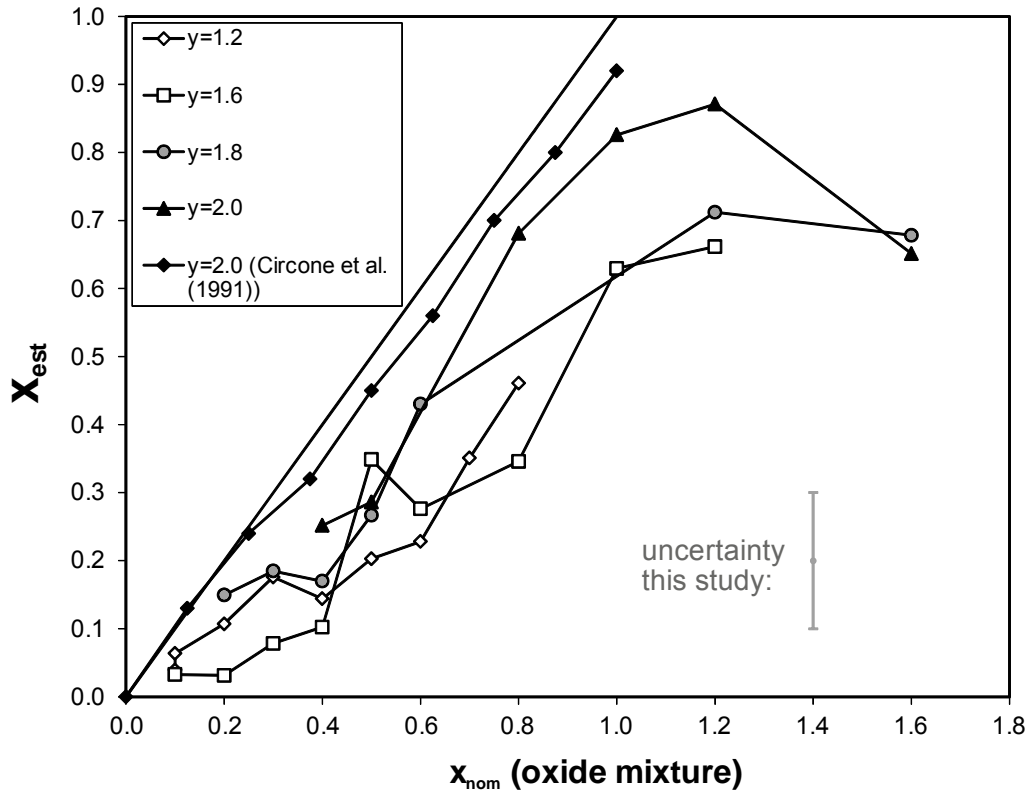
822

823

824

Revision #3

825 Figure 2

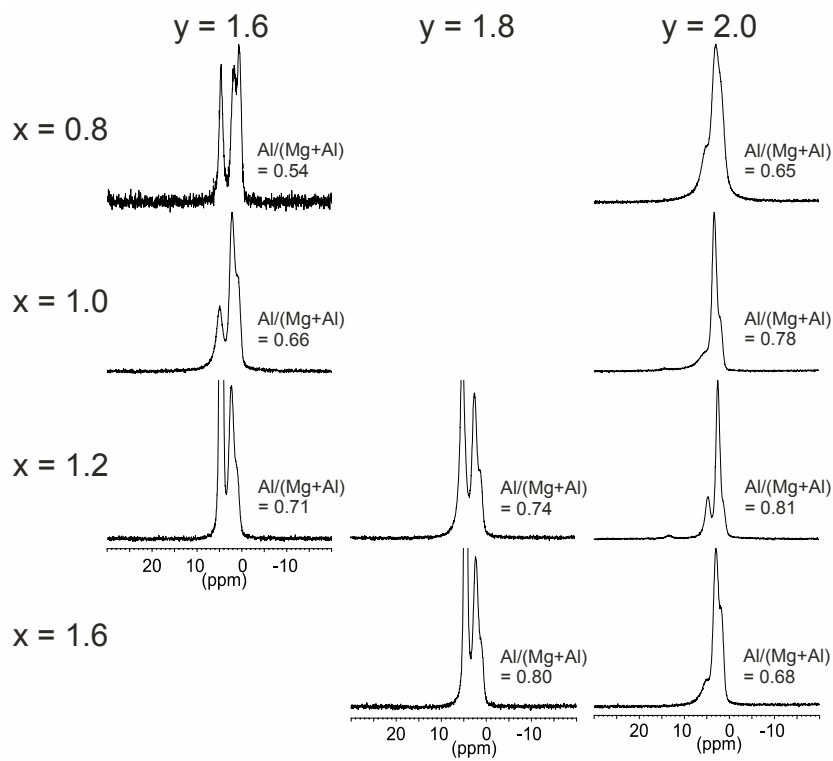


826
827
828
829

Revision #3

830 Figure 3

831

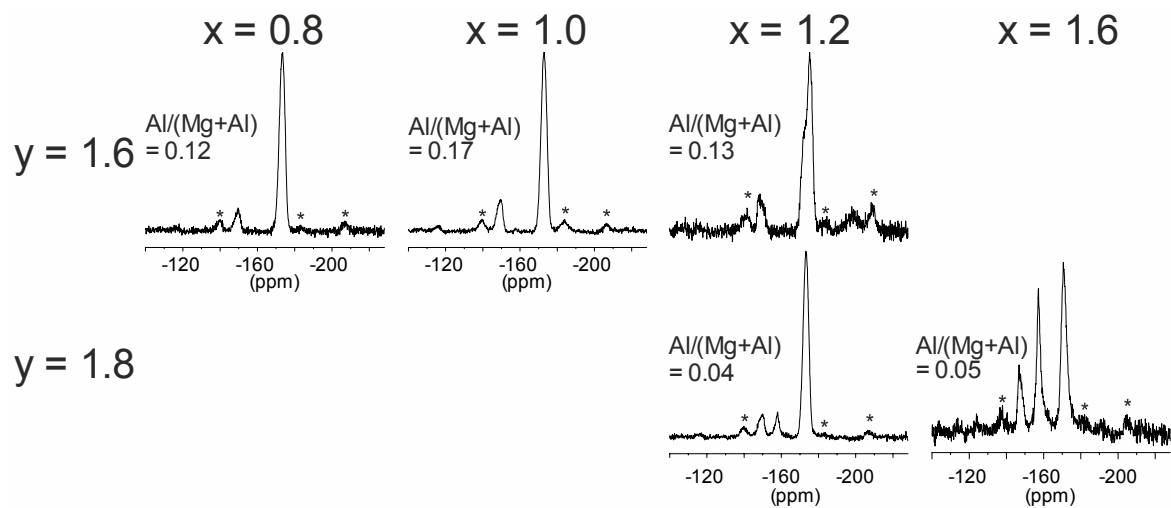


832

833

Revision #3

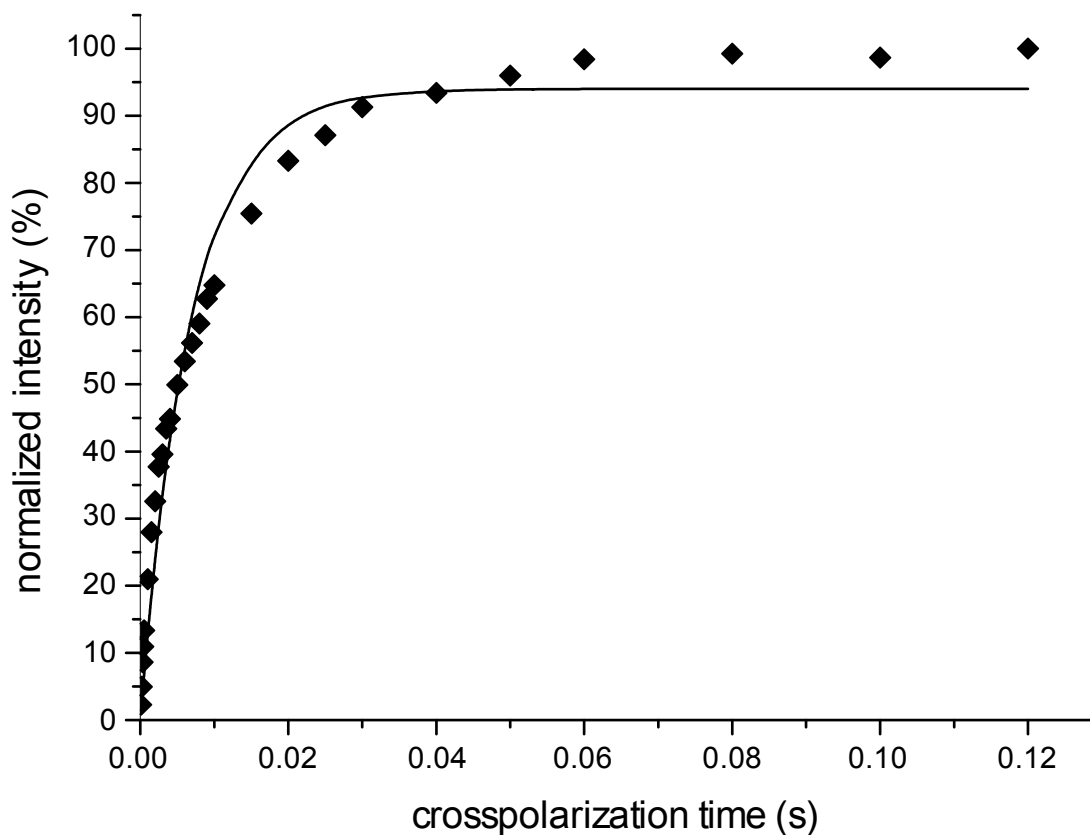
834 Figure 4
835
836



837
838
839

Revision #3

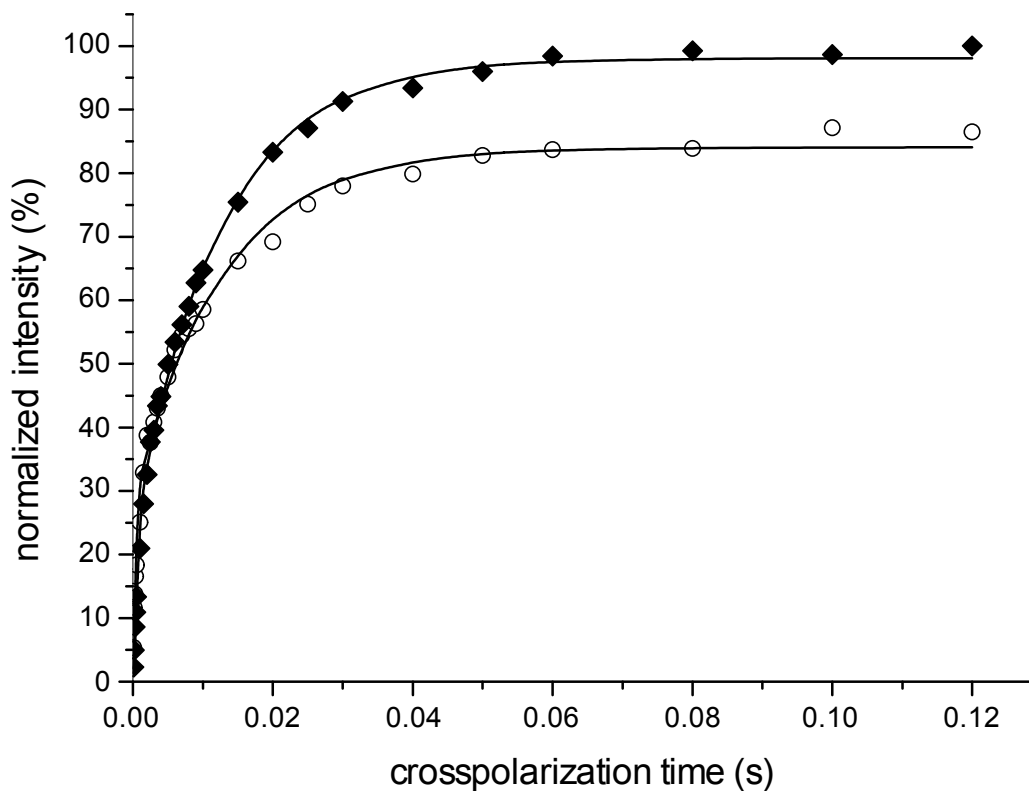
840 Figure 5
841



842
843
844

Revision #3

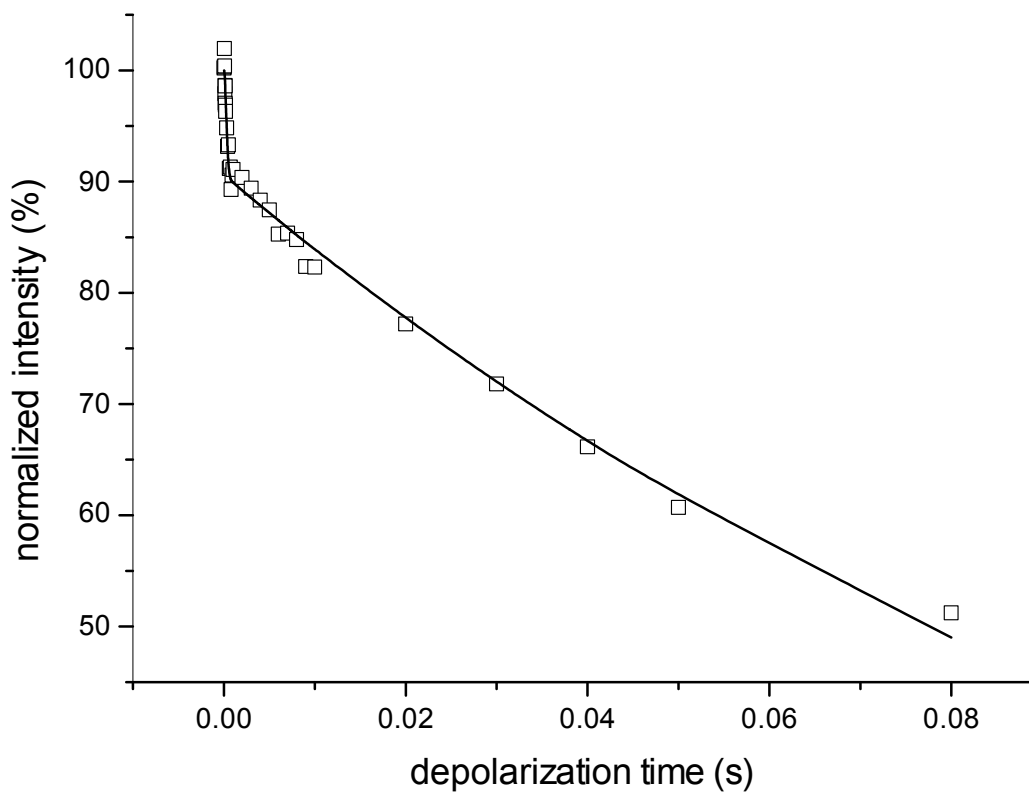
845 Figure 6
846



847
848

Revision #3

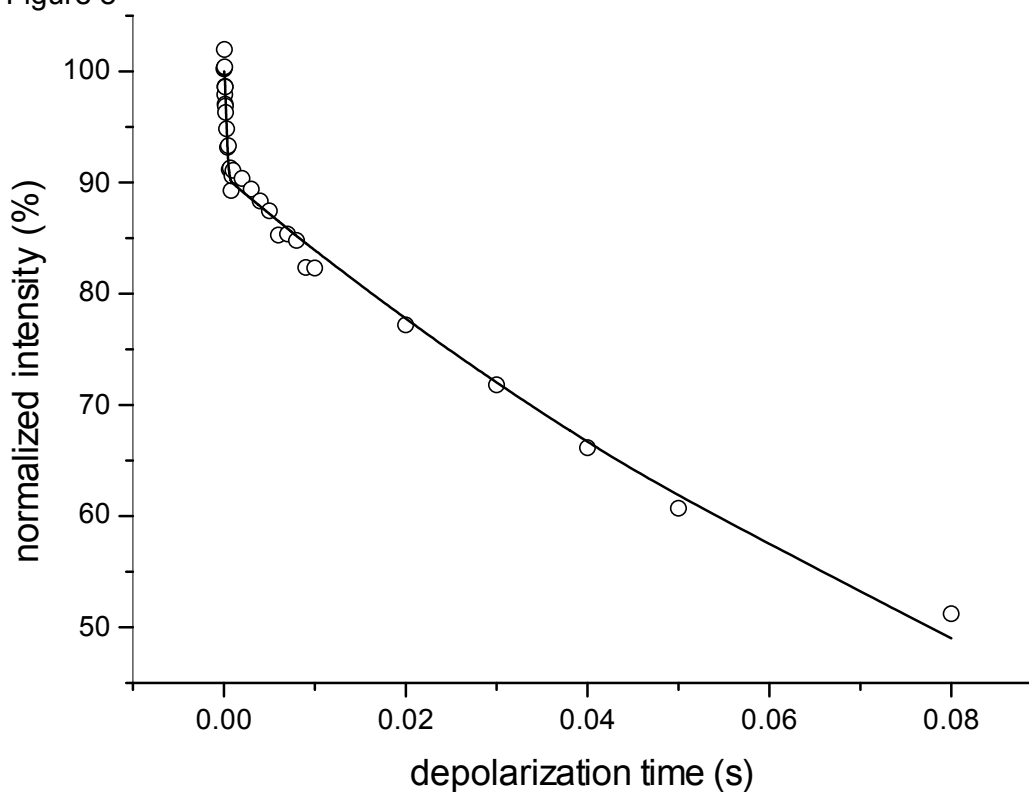
849 Figure 7
850



851
852

Revision #3

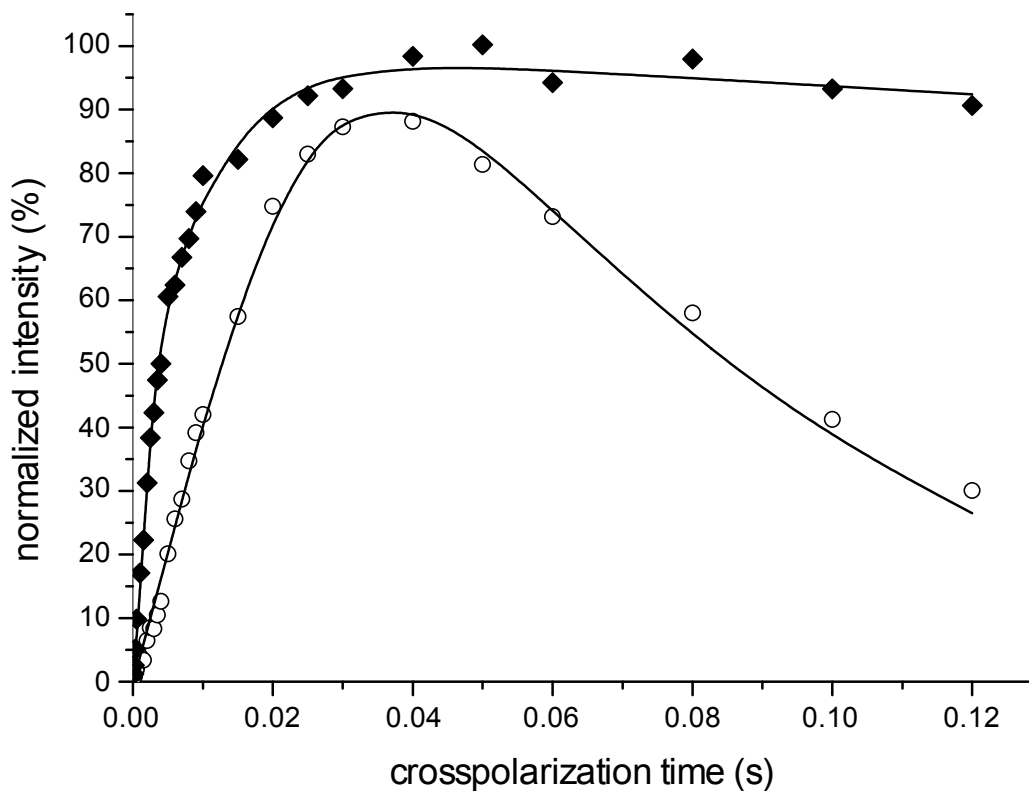
853 Figure 8



854
855

Revision #3

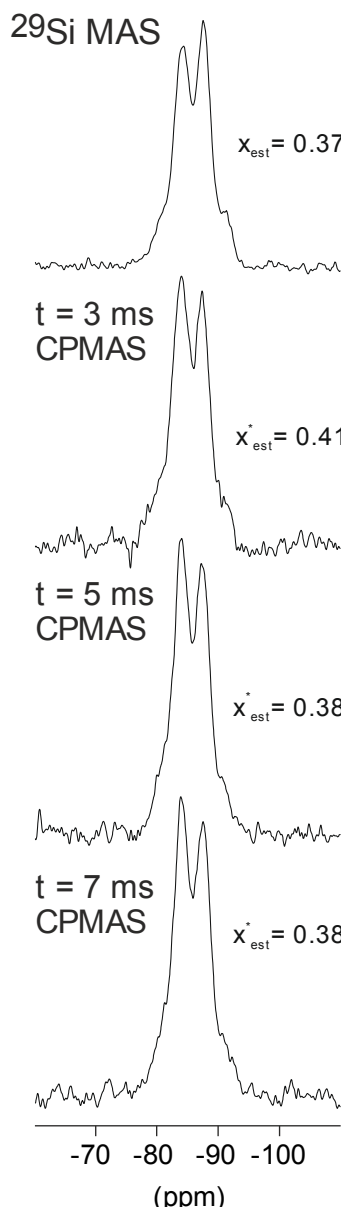
856 Figure 9
857



858
859

Revision #3

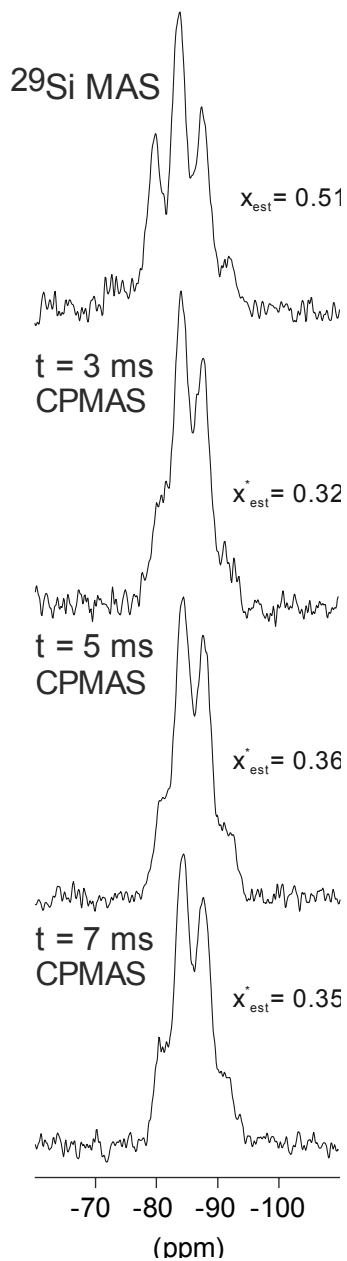
860 Figure 10
861



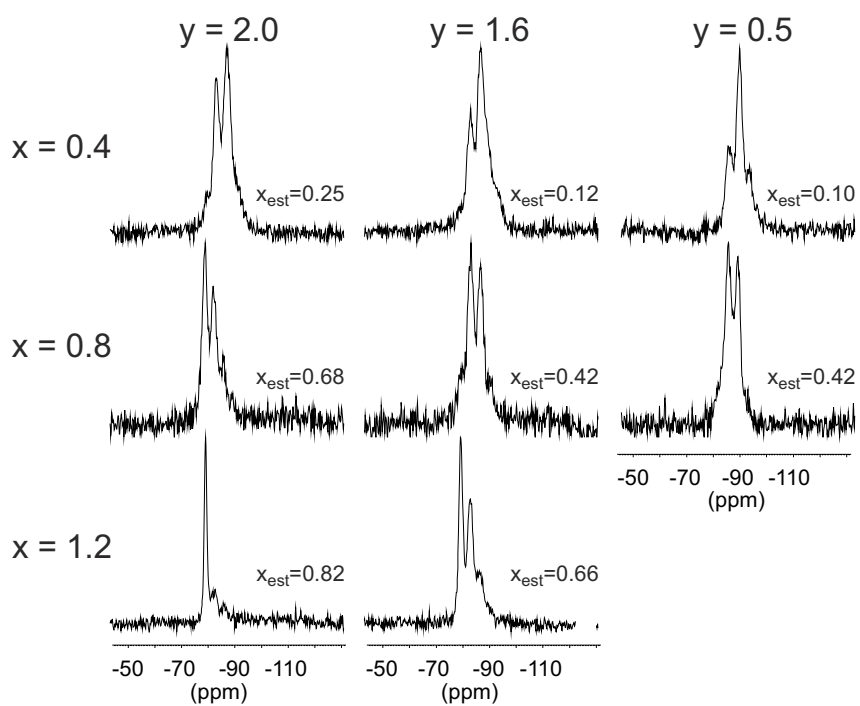
862
863
864

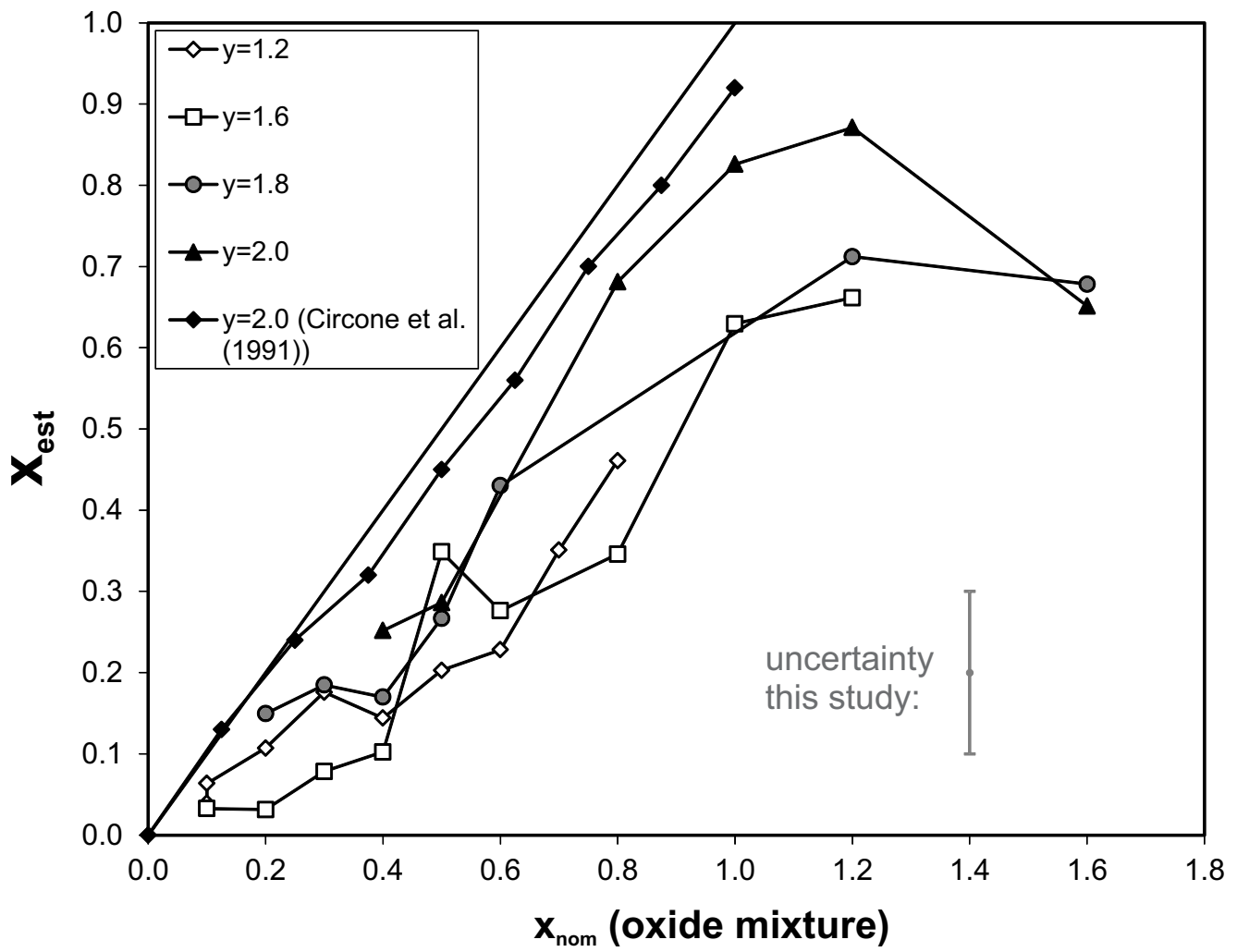
Revision #3

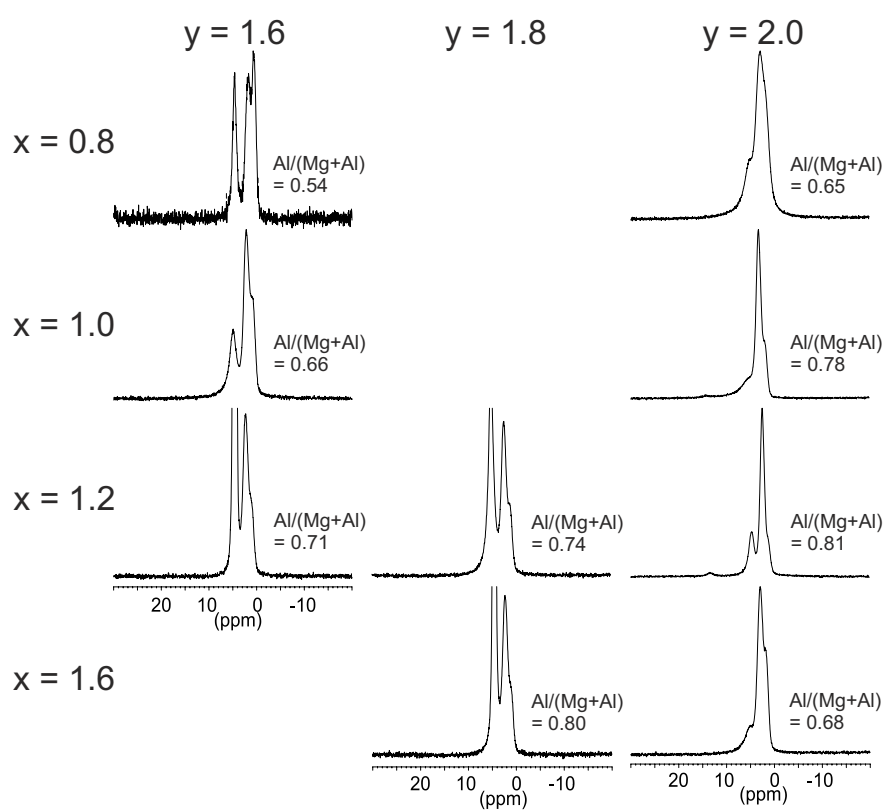
865 Figure 11
866

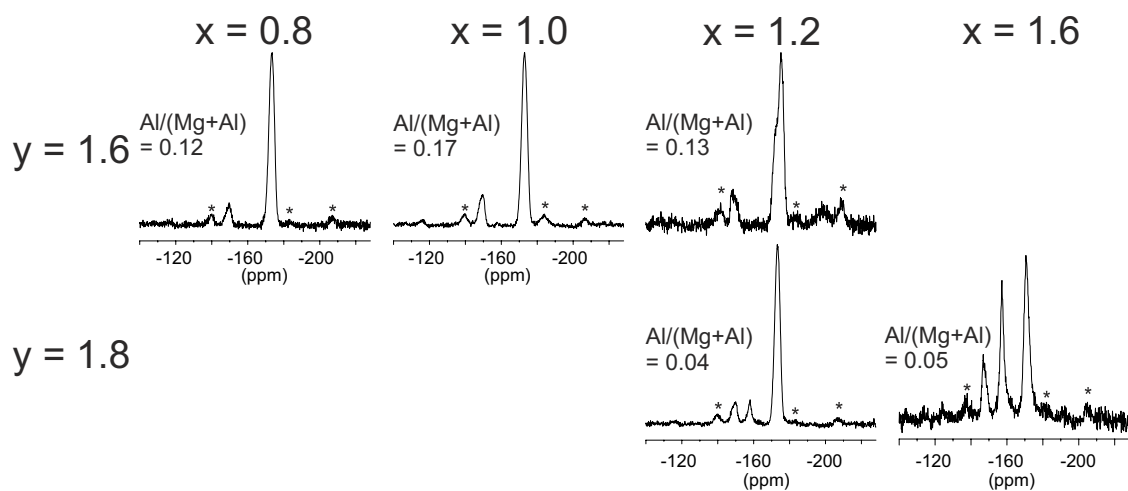


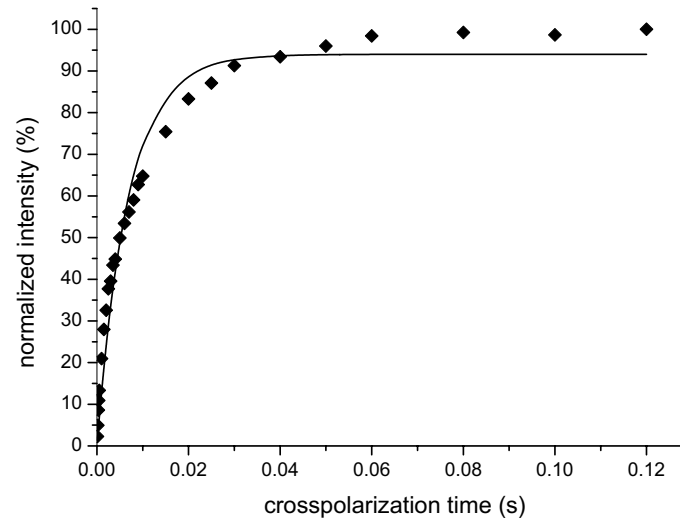
867
868
869
870

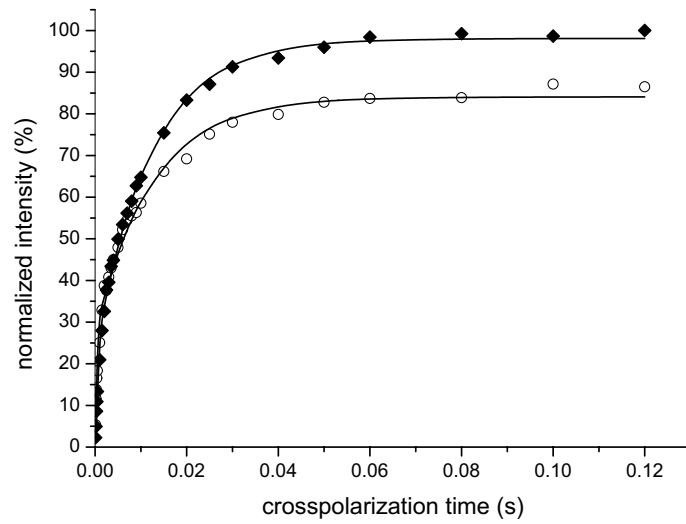


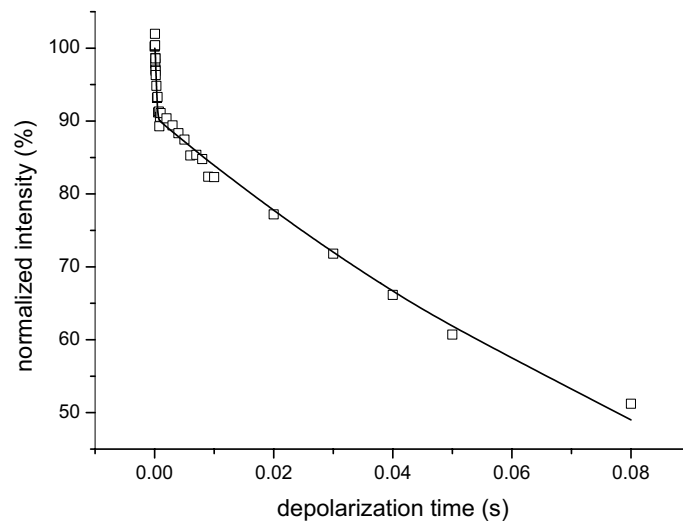


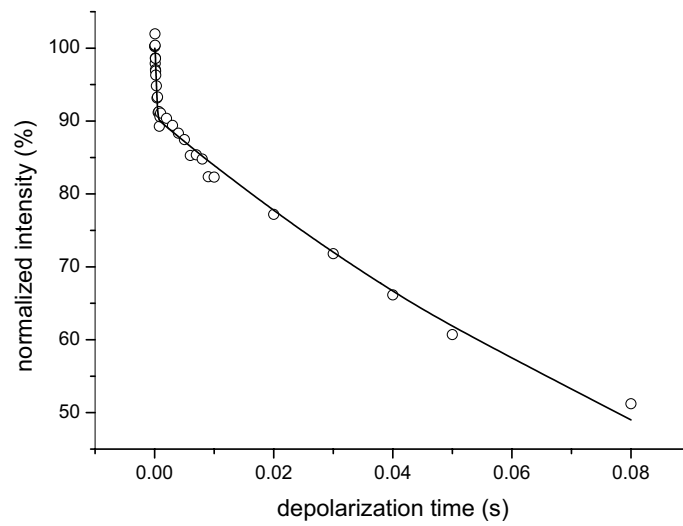


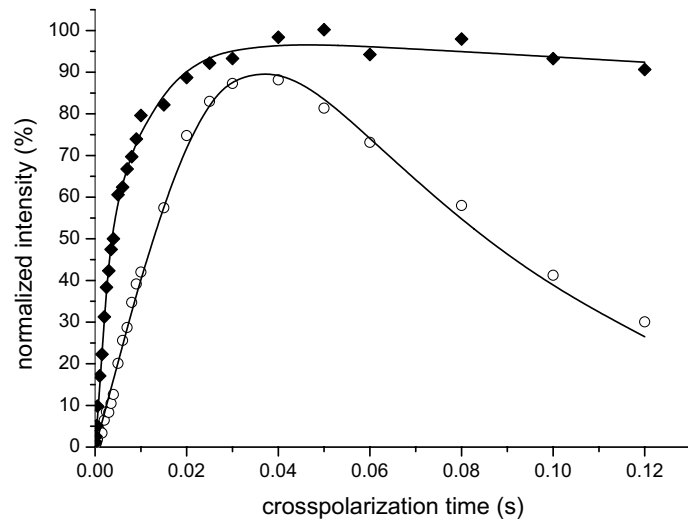


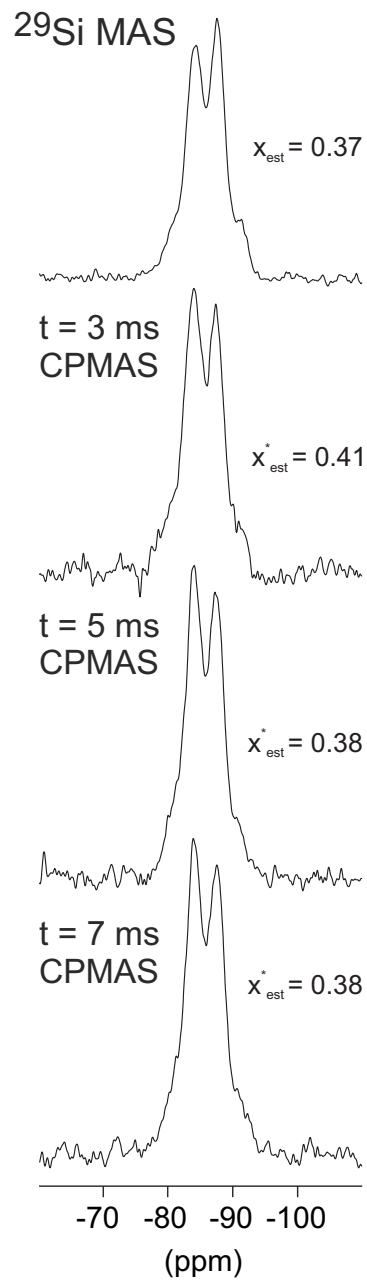






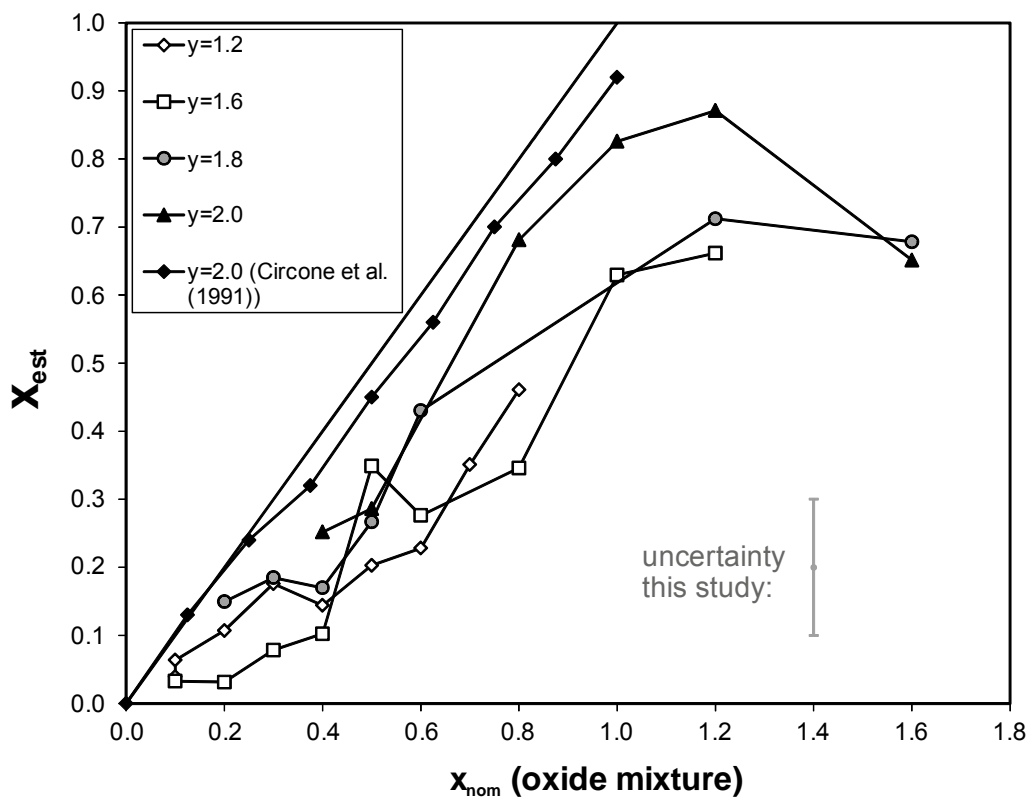






Revision #3

825 Figure 2



826
827
828
829